Journal of Innate Immunity

Research Article

J Innate Immun
DOI: 10.1159/000524587

Received: January 20, 2022
Accepted: March 8, 2022
Published online: May 12, 2022

Development, Characterization, and in vivo Validation of a Humanized C6 Monoclonal Antibody that Inhibits the Membrane Attack Complex

Heidi Gytz Olesen[a] Iliana Michailidou[b] Wioleta M. Zelek[c] Jeroen Vreijling[b] Patrick Ruizendaal[d] Ferry de Klein[d] J. Arnoud Marquart[e] Thomas B. Kuipers[f] Hailiang Mei[f] Yuchun Zhang[g] Muhammad Ahasan[g] Krista K. Johnson[g] Yi Wang[g] B. Paul Morgan[c] Marcus van Dijk[h] Kees Fluiter[b] Gregers Rom Andersen[a] Frank Baas[b, h]

[a]Department of Molecular Biology and Genetics – Protein Science, Aarhus University, Aarhus, Denmark; [b]Department of Clinical Genetics, LUMC, Leiden, The Netherlands; [c]Division of Infection and Immunity and Dementia Research Institute, Systems Immunity Research Institute, School of Medicine, Cardiff University, Cardiff, UK; [d]Core Facility Genomics, Amsterdam UMC, Amsterdam, The Netherlands; [e]Molecular Hematology, Amsterdam, The Netherlands; [f]Sequencing Analysis Support Core, Department of Biomedical Data Sciences, LUMC, Leiden, The Netherlands; [g]Alexion, AstraZeneca Rare Disease, New Haven, CT, USA; [h]Complement Pharma BV, Amsterdam, The Netherlands

Keywords
Complement system · Complement component 6 · Membrane attack complex · Monoclonal antibody

Abstract
Damage and disease of nerves activates the complement system. We demonstrated that activation of the terminal pathway of the complement system leads to the formation of the membrane attack complex (MAC) and delays regeneration in the peripheral nervous system. Animals deficient in the complement component C6 showed improved recovery after neuronal trauma. Thus, inhibitors of the MAC might be of therapeutic use in neurological disease.
Here, we describe the development, structure, mode of action, and properties of a novel therapeutic monoclonal antibody, CP010, against C6 that prevents formation of the MAC in vivo. The monoclonal antibody is humanized and specific for C6 and binds to an epitope in the FIM1-2 domain of human and primate C6 with sub-nanomolar affinity. Using biophysical and structural studies, we show that the anti-C6 antibody prevents the interaction between C6 and C5/C5b by blocking the C6 FIM1-2:C5 C345c axis. Systemic administration of the anti-C6 mAb caused complete depletion of free C6 in circulation in transgenic rats expressing human C6 and thereby inhibited MAC formation. The antibody prevented disease in experimental autoimmune myasthenia gravis and ameliorated relapse in chronic relapsing experimental autoimmune encephalomyelitis in human C6 transgenic rats.
CP010 is a promising complement C6 inhibitor that prevents MAC formation. Systemic administration of this C6 monoclonal antibody has therapeutic potential in the treatment of neuronal disease.

Heidi Gytz Olesen, Iliana Michailidou, Wioleta M. Zelek, Gregers Rom Andersen, and Frank Baas contributed equally.

Karger@karger.com
www.karger.com/jin

Correspondence to:
Frank Baas, f.baas@lumc.nl

Introduction

Complement (C) activation is a common feature in neurodegenerative diseases such as Alzheimer's disease, multiple sclerosis (MS), Parkinson's disease, Huntington's disease, and amyotrophic lateral sclerosis [1, 2]. During neurodegeneration, there is aberrant activation of C in areas of pathology, leading to activation of the terminal pathway, which ultimately drives the formation of the membrane attack complex (MAC) as outlined in Figure 1a. MAC is an important innate immune effector that is inserted in the membrane of the target cell [3, 4]. MAC formation is initiated when the complement component 5 (C5) is cleaved by the C5 convertase enzyme into the small C5a fragment, a potent anaphylatoxin, and C5b. The larger, labile fragment C5b is captured in a stable conformation by sequentially binding to C6 and C7, leading to formation of the stable C5b67 complex. The C5b-7 complex is released from the convertase, then binds tightly to an adjacent membrane, and forms a platform for completion of MAC assembly. Inclusion of C8 and multiple copies of C9 causes a stepwise insertion of the forming MAC into the target membrane to form a lytic pore [5]. On nucleated host cells, sub-lytic amounts of MAC may instead trigger pro-inflammatory responses [6, 7].

MAC causes damage after neurotrauma [8, 9] and in neurodegenerative disease [10, 11]. We earlier demonstrated that C6 deficiency in a rat model of nerve crush facilitated nerve regeneration, whereas add-back of human C6 (hC6) restored MAC formation and delayed nerve regeneration to the slow level seen in wild-type animals [12, 13]. This demonstrates that systemic C6 affects neuroaxonal recovery [14]. We earlier performed pharmacological inhibition of hepatic C6 production using systemically delivered antisense oligonucleotides and tested this in three models; brain trauma [15], nerve damage [16], and chronic relapsing experimental autoimmune encephalomyelitis (crEAE) [17]. In all three disease models, downregulation of hepatic C6 synthesis reduced plasma C6 levels, reduced MAC formation, and prevented macrophage influx at sites of injury, thus promoting recovery. The data suggest that C6 levels in the circulation are a limiting factor for the formation of MAC in the PNS and CNS; therefore, targeting C6 for specific inhibition of MAC assembly is a promising approach to mitigate exacerbation or progression in nervous system disease. MAC inhibition leaves the upstream components of the C system intact, minimizing the adverse effects which may occur due to C interactions with immune defence and elimination of debris [18–20].

So far, the only therapy-approved monoclonal antibodies blocking MAC formation are the anti-C5 antibody eculizumab and its long-acting version ravulizumab [21]. Both eculizumab and ravulizumab bind specifically to human C5 and prevent its cleavage into C5a and C5b by the C5 convertase. However, the anaphylatoxin C5a is a modulator of innate and adaptive immune responses, and therefore, inhibition of C5a by an anti-C5 antibody may delay regeneration and halt recovery in some disease contexts [22–24].

Based on our results from studies on C6 deficiency [12, 13] and the use of C6 antisense oligonucleotides in brain and nerve pathologies [15–17], we hypothesized that C6 would be an ideal molecule to target in order to block MAC in these conditions. Since C6 has no known function apart from being a component of MAC, inhibition of C6 would only affect MAC formation, leaving other parts of the C system, and other arms of the tightly linked immune system, unaffected. The aim of this study was to develop a monoclonal antibody that specifically blocks MAC formation by targeting C6 and to describe its structure, mode of action, and in vivo efficacy.

Here, we present a humanized monoclonal antibody that binds human and primate C6 to inhibit MAC formation in vitro and in vivo and in C6-humanized rats, prevented disease in the experimental autoimmune myasthenia gravis (EAMG) model and mitigated relapse in a model of relapsing experimental autoimmune encephalitis (EAE). We describe the epitope-paratope interactions in detail and present a model for the antibody's mode of action. This report demonstrates and fully characterizes a monoclonal antibody targeting C6 that blocks MAC function and has considerable potential for therapeutic application in afflictions where MAC activation is contributing to disease progression.

Materials and Methods

Selection and Production of the C6 Monoclonal Antibody

Generation of C6 Affinity Columns

To generate anti-C6 affinity columns, the C6-binding MAbs (23D1, 20D2, and CP010) were diluted in coupling buffer (0.2 M Na_2HCO_3, 0.5 M NaCl [pH 8.3]), immediately injected into a preactivated 1 mL or 5 mL HiTrap N-hydroxysuccinimide-activated high-performance column (GE Healthcare), and incubated for 1 h at room temperature. The column was blocked with 0.5 M ethanolamine (pH 8.3) and washed into running buffer (HEPES containing 0.5 M NaCl); column eluate was retained to measure unbound antibody (bicinchoninic acid assay; Thermo Fisher); coupling efficiency was >90%. The non-blocking mouse anti-hC6 antibodies 23D1 and 20D2 were generated in house by immunization of C6-deficient mice.

C6 Isolation

Native C6 for immunization was isolated from human serum donated by healthy volunteers. Serum was passed over a 23D1 anti-C6 column and bound C6 eluted with 0.1 M glycine (pH 2.5). The C6 was further purified by Mono Q 5/50 anion exchange chromatography and eluted with a NaCl gradient to 1 M NaCl in 10 mM KH_2PO_4 (pH 7.8). Protein-containing fractions were collected, pooled, and dialysed overnight at 4°C into HEPES-buffered saline (HBS) containing 0.5 M NaCl. Dialysed protein was aliquoted and stored at −80°C. For all other experiments, C6 was isolated by immunoaffinity purification on anti-C6 columns generated using either 25 mg of the mouse monoclonal anti-hC6 antibodies (clones 23D1 or 20D2) or 5 mg of CP010. Protein purity was confirmed by SDS-PAGE analysis.

Haemolytic Assay

The inhibitory activity of the anti-C6 mAbs was investigated by classical pathway haemolysis assay (CP; CH50) using antibody-sensitized sheep erythrocytes; sheep blood was from TCS Bioscience, and anti-sheep antiserum (#ORLC25; Siemens Amboceptor) was from Cruinn Diagnostics (Dublin, UK). Antibody-sensitized sheep erythrocytes were suspended in HBS containing Ca^{2+} and Mg^{2+} at 2% (vol/vol). A serial dilution series of CP010 (100–0 μg/mL; 50 μL/well) was prepared in HBS and aliquoted in triplicate into a 96-well round-bottomed plate at 50 μL/well, and then normal human serum added to the plates at 2.5% in HBS (50 μL/well). In some experiments, normal human serum depleted of C6 (C6D) was mixed with C6 purified on CP010 or 20D2 (50 μg/mL undiluted C6D) and tested as above. Serum dilution 2.5% was selected in preliminary experiments to give near-complete haemolysis in the CP assay in the absence of test mAb. Plates were incubated at 37° for 30 min, centrifuged, and haemoglobin in the supernatant was measured by absorbance at 405 nm. Percentage lysis was calculated according to: %Lysis = (Absorbance [Abs] sample − Abs background)/(Abs max − Abs background) × 100%. GraphPad Prism was used for data analysis (GraphPad Software, San Diego, CA, USA).

C9 Deposition ELISA

ELISA wells (flat-bottom 96-well plates, high binding; Greiner Bio-One – 655061) were coated with Mannan (Sigma; 10 μg/mL in 100 μL coating buffer, 15 mM Na_2CO_3, 35 mM $NaHCO_3$, 15 mM NaN_3 [pH = 9.6]) as a trigger for the lectin pathway activation in the presence of human serum. After washing, they were blocked by incubation with blocking buffer (100 μL; 1 mg/mL BSA, 145 mM NaCl, 15 mM NaN3, 10 mM Tris/HCl, pH 7.4). A serial dilution series of the test compound was made in dilution buffer (94 mM barbital, 145 mM NaCl, 2 mM $CaCl_2$, 1 mM $MgCl_2$, 0.3% BSA, 0.02% Tween 20) and added to the plates. Human serum was added (1:100 in dilution buffer) as a complement source. The action of the inhibitor was monitored by detection of the level of C9 deposition on the plate which was detected by anti-C5b-9neo (clone aE11; DAKO: M0777). Anti-mouse HRP (DAKO: P0447) was used as the secondary antibody, visualized by enzymatic reaction in the presence of a chromogen and TMB substrate (10 mg/mL; 3,3′,5,5′-tetramethylbenzidine liquid substrate; Sigma T4444).

Animal Immunization Protocol

All animals were fed ad libitum and were housed in normal 12 h day/night cycles. C6-deficient rats (PVG $C6^{-/-}$) were immunized with the hC6 protein. C6-deficient rats are expected to show a robust antibody response to C6 immunization since they lack the protein and therefore "see" C6 as completely "foreign." Immunization was done in compliance with the Dutch code of practice for immunization (*Werkgroep immunisatieprocedures Keuringsdienst van Waren, aangepaste tweede versie Augustus 2000*) by subcutaneous injections at four sites on the flanks with purified C6 (100 μg) in complete Freund's adjuvant (CFA; Sigma-Aldrich, St Louis, MO, USA), total volume 250 μL per injection. Booster injections were given 14 and 21 days after the first immunization with 50 μg of antigen in incomplete Freund's adjuvant (Sigma-Aldrich). Animals received two additional booster injections intravenously at day 62 and 64 using 100 μg of antigen in PBS and were humanely killed at day 66 to obtain blood and spleen.

Lymphocytes were isolated from the spleen using standard protocols, mixed with fusion partner cells (Y3) in fusion media, and fused using a standard protocol with polyethylene gylcol PEG-fusion (ModiQuest BV, Oss, the Netherlands). Immediately following the fusion event, cells were seeded in 96-well plates in medium containing hypoxanthine, aminopterin, and thymidine for hybridoma selection.

Antibody Selection and Purification

Supernatants of all hybridomas were screened using a standard antigen-specific ELISA on hC6-coated ELISA plates. Sixteen clones were selected for 2 rounds of subcloning resulting in 5 subclones from different original clones with good growth properties and C6 antibody production. Antibody production was scaled up for selected hybridomas, and the antibody was purified from medium using Protein G GraviTrap columns (GE Healthcare). SDS-PAGE and size exclusion chromatography (SEC) were used for quality control. Antibodies were stored in Dulbecco's PBS (Lonza).

5′ Rapid Amplification of cDNA Ends and Sequencing of Variable Heavy Chain and Variable Light Chain Regions

One rat hybridoma clone (7E5) proved superior in the CH50 assay and was selected for 5′ rapid amplification of cDNA ends (RACE) [25] and sequencing. The repertoires were amplified using standard PCR and 5′ RACE primers [26]. The resulting samples were gel-purified to the expected lengths and pooled for sequencing. Both 7E5-VH and -VL cDNAs obtained from the nested PCR were cloned. Of each population of cloned cDNAs, $2\times n = 16$ clones were tested for full-length inserts and $2\times n > 8$ full-length clones per population were submitted for sequence analysis. In total, $n = 21$ variable heavy chain (VH) clones and $n = 26$ variable light chain (VL) clones were sequenced. The consensus VH and VL sequences were recloned into a mouse IgG1 framework and retested. This clone showed similar binding properties to the original hybridoma.

Humanization

PCR-based humanization for both VH and VL sequences of the selected antibody was performed at FairJourney Biologics (Porto, Portugal) according to the method of Hwang et al. [27]. Humanization and in-solution C6-based affinity purification of combinatorial phage display libraries were used to identify humanized clones and to select for increased affinity. Fabs were expressed in *E. coli*, and a lead panel of 9 humanized Fabs with human identity and homology percentage values varying from 90 to 99% and similar off-rates to the parental 7E5 antibody as measured by surface plasmon resonance (SPR) (with C6 solid phase) was selected for

further functional testing in CH50 assays. The separate heavy and light chains were cloned on the human IgG4 S228P constant region, and all 81 combinations were expressed in *E. coli*. Expression levels varied, and the combination with the highest expression and strongest inhibition in CH50 was selected. Clone 7E5-MPO7E12 was selected and designated CP010.

Production of the Humanized C6 Monoclonal Antibody and Isotype Control Antibody

For the in vivo experiments, the VL and VH domains of the humanized version of the rat C6 monoclonal antibody and an isotype control antibody were expressed on a rat IgG2c constant region (Evitria, Zurich, Switzerland). As the isotype control, we used the MOTA antibody which targets a highly conserved epitope in the A antigenic site of the RSV fusion (f) protein [28]. Both antibodies were modified to prevent binding to Fcγ receptors and complement activation by using a NALAPG motif together with the P329G mutation [29]. The VH and VL sequences of the 7E5 NALAPG and MOTA NALAPG antibodies are provided in online supplementary Table 1 (for all online suppl. material, see www.karger.com/doi/10.1159/000524587).

Recombinant Protein Expression and Purification

C6

Expression plasmids encoding hC6 (Uniprot entry: P13671) with a C-terminal 10xHis-tag, and a C6 fragment encompassing the two FIM domains (residues 766–934) with an N-terminal 10xHis-tag were designed using the endogenous Kozak sequence and signalling peptide. The constructs were obtained by gene synthesis and subcloned using *Hin*dIII and *Bam*HI restriction sites into pcDNA3.1(+) by Genscript. Truncated C6 variants were prepared by site-directed mutagenesis using the QuickChange Lightning kit (Agilent Technologies, Santa Clara, CA, USA). A minimal C6 FIM1-2 construct (10xHis-TEV-769-934) was made by introducing a TEV cleavage site after the His-tag. The following C6 variants with the canonical signal peptide and C-terminal His-tags were prepared: C6ΔFIM1-2 (1–762) and FIM1-2. An Asn-linked glycan was removed by site-directed mutagenesis changing Asn855 to Ala. DNA encoding FIM1-2 variants from non-human animals (Macaca: tr|A0A2K5W3S5, dog: XP_022273595.1 and *Sus scrofa* [pig]: NP_001090918.1) were designed with an N-terminal His-tag and the hC6 signalling peptide and prepared by GenScript. All plasmids for transfection were prepared using the QIAGEN Midi-Prep kit according to manufacturer's recommendation.

Recombinant C6 variants were expressed in HEK293f cells maintained at 37°C, 8% CO_2 in shaking culture (125 rpm) in serum-free FreeStyle 293 Expression Medium (Invitrogen, Carlsbad, CA, USA). Cells were transiently transfected using final concentrations of 2 mg/L polyethylenimine (PEI – 25 kDa; Polysciences, Touhy Avenue Niles, IL, USA) and 1 mg/L plasmid DNA. The conditioned medium was harvested 5 days post-transfection and adjusted to pH 8 with 50 mM Tris-HCl. The secreted C6 variants were purified on a 5-mL HisTrap (GE Healthcare) column followed by SEC on a 24-mL Superdex 200 increase column (GE Healthcare) equilibrated in 20 mM HEPES (pH 7.5), 150 mM NaCl. Yields were generally high, ranging from 5 to 17 mg from 500 mL conditioned medium.

For site-specific biotinylation of C6 and C6ΔFIM1-2, an AVI-tag (GLNDIFEAQKIEWHE) was introduced at the N-terminal after the signal peptide with the QuikChange Lightning Site-Directed Mutagenesis Kit (Agilent Technologies). AVI-tagged proteins were purified as described above and supplemented with 0.15 mM biotin, 2 mM ATP, and 5 mM $MgCl_2$. BirA ligase was added at 1:10 wt/wt ratio, and biotinylation was carried out for 18 h at 25°C. The sample was 0.22-μm filtered, and the C6 protein separated from BirA and excess ATP on a 24-mL Superdex 200 increase SEC column equilibrated in 20 mM Hepes (pH 7.5), 150 mM NaCl.

CP010 Fab

The Fab fragment of CP010 (IgG4) was prepared by limited proteolysis and reduction. Firstly, $F(ab)_2$ fragments were made by incubating 100 mg of the CP010 antibody with 2 mg freshly prepared and activated papain (Sigma-Aldrich; P4762) in 10 mM cysteine, 1.25 mM EDTA, and the reaction was incubated overnight at room temperature. The reaction was stopped by incubation with 30 mM iodoacetamide for 30 min at 37°C. The resulting $F(ab)_2$ and Fc fragments were concentrated, filtered, and buffer-exchanged before loading on a 120-mL Superdex 200 PG (GE Healthcare) SEC column equilibrated in 150 mM NaCl, 20 mM Hepes (pH 7.5). To generate Fab, $F(ab)_2$ fractions were pooled and subjected to partial reduction in 0.11 mM DTT, 3.5 mM EDTA, 170 mM Tris (pH 7.5) for 45 min at room temperature. The reaction was stopped by addition of 10 mM iodoacetamide, and the resulting Fab was separated from residual $F(ab)_2$ on a 24-mL Superdex S200 increase SEC column equilibrated in 20 mM HEPES (pH 7.5), 150 mM NaCl.

κ Nb

An expression plasmid for the anti-κ light-chain nanobody (described in patent WO2006059904A1) was a gift from Dr. Michaela Miehe. An internal V5 tag was removed by site-directed mutagenesis, leaving the pelB leader sequence for periplasmic secretion and a C-terminal 6xHis-tag. The κ Nb was expressed in *E. coli* BL21(DE3), grown at 37°C in LB broth; protein expression was induced when OD600 reached ~0.6 by addition of 0.5 mM isopropyl β-D-1thiogalactopyranoside. Growth was continued overnight at 18°C. The cell pellet was resuspended in 20 mM Tris-HCl (pH 8), 500 mM NaCl, 1 mM EDTA, and 1 mM PMSF and lysed by sonication. Cell debris was removed by centrifugation, and supernatant loaded on a 5-mL HisTrap column (GE Healthcare), washed with lysis buffer, supplemented with 25 mM imidazole, and the protein was eluted with 500 mM imidazole. The eluted protein was dialysed against 20 mM acetate (pH 5.5), 50 mM NaCl overnight at 4°C then applied to a 1-mL Source 15S (GE Healthcare) cation exchange column equilibrated in 20 mM acetate (pH 5.5), 50 mM NaCl. Bound protein was eluted in a 40-mL linear gradient from 20 to 500 mM NaCl.

C5 C345c

An expression plasmid encoding the human C5 C345c domain (Uniprot entry P01031, residues 1528–1676) with an N-terminal 10xHis-tag and the endogenous C5 signalling peptide in pcDNA3.1 was prepared by amplification of the insert from a bacterial expression vector by PCR and the PfuUltra II Hotstart PCR Master Mix (Agilent Technologies) according to the manufacturer's recommendations. The amplified insert was gel-purified and used as a megaprimer on the pcDNA3.1 His-FIM1-2 template described above, and the final construct was obtained by mutagenesis using the Phusion High-Fidelity DNA Polymerase (Thermo Fisher Scientific, Waltham, MA, USA). Expression and purification were carried out as described for the recombinant C6 variants.

Purification of human C5 from outdated plasma and CVF from *Naja naja* siamensis venom were done as described [30, 31]. Human factor B and factor D were purchased from Complement Technology.

Crystallization and Structure Determination

The ternary complex CP010 Fab:FIM1-2 N855A:κ Nb was formed by incubating Fab with a molar excess of FIM1-2 and κ Nb at room temperature before purification on a 24-mL Superdex 200 increase column (GE Healthcare). Crystals were grown at 19°C in hanging drops made by mixing 0.5 µL of the SEC purified complex concentrated to 10–23 mg/mL with 0.5 µL reservoir solution, followed by immediate streak seeding. The best crystals grew to a maximum size of 300 × 300 × 100 µm over a reservoir containing 112 mM calcium acetate, 56 mM sodium cacodylate (pH 6.4), 8.5% PEG8000, and 16% glycerol. Crystals were cryoprotected in the undiluted mother liquor before flash cooling in liquid nitrogen. Data were collected at the MAX IV beamline BioMAX using radiation with λ = 0.9762 Å at 100 K and processed with XDS [32] to 2.3 Å. A library of ~2,000 Fab search models was prepared by identification of unique Fab structures in the SabDab database [33] and screened by molecular replacement with phenix.phaser [34]. The model with the highest TFZ and LLG scores was the pinatuzumab Fab in complex with an anti-κ VHH domain (PDB entry 6AND). The initial model was completed in phenix.phaser by searching with the individual FIM2 and FIM1 domains from the PDB entry 3T5O. The resulting model was refined with a rigid body refinement in phenix.refine [35]. The structure was manually rebuilt in Coot [36] and refined with phenix.refine in an iterative manner using positional refinement, individual B-factors, and TLS groups. Structure analysis and figure preparation were done with PyMol (www.pymol.org).

Bio-Layer Interferometry

Biolayer interferometry (BLI) experiments were carried out using an Octet Red96 (ForteBio, Fremont, CA, USA) at 30°C with shaking at 1,000 rpm. The running buffer for all experiments was 20 mM HEPES, 150 mM NaCl supplemented with either 0.05% Tween 20 or 1 mg/mL bovine serum albumin, respectively.

CP010 Fab affinity measurements were conducted with full-length C6 or the FIM1-2 fragment as follows. For full-length C6, streptavidin biosensors (ForteBio) were loaded in a solution containing 3 µg/mL biotinylated C6, and the CP010 Fab was present in a 2-fold dilution series from 25 to 0.39 nM in the association phase. For the His-tagged FIM1-2 variants, PentaHis sensors were loaded in a solution of 10 µg/mL FIM1-2, and the CP010 Fab was present in a 2-fold dilution series from 50 to 1.56 nM in the association phase. After dissociation, the sensors were regenerated with 10 mM glycine (pH 2.3), 1 M NaCl before recharging. The data were processed by subtraction of a 0-nM measurement using the Octet System Data Analysis software (ForteBio) and fitted globally with a 1:1 Langmuir binding model using GraphPad Prism Software.

For the C5 and C5 C345c binding assays, 50 µg/mL C5 or 15 µg/mL C5 C345c was immobilized on amine reactive second-generation (AR2G) biosensors in 10 mM sodium acetate (pH 5), 25 mM NaCl. The sensors were quenched with 1 M ethanolamine, pH 8.5, and equilibrated in running buffer. The signal from sensors without the relevant C6 variant and the maximum CP010 Fab concentration used in the experiment were subtracted as background. For C6 affinity measurements, C5 C345 coated sensors were immersed in wells containing a 2-fold dilution series of C6 ranging from 125 to 7.8 nM and vice versa for biotinylated C6 coated sensors with C5 C345c in the well. For FIM1-2 affinity measurements, wild-type C5 C345c was immobilized on AR2G sensors as described before and associated with 12.5, 25, and 50 nM FIM1-2.

Complex formation with C5b was investigated by pre-assembly of the fluid phase C5 convertase CVFBb containing 100 nM CVF, 100 nM factor B, and 10 nM factor D in activation buffer (20 mM Tris [pH 7.5], 50 mM NaCl, 5 mM $MgCl_2$). The solution was incubated at 37°C for 15 min. Next, streptavidin biosensors were coated with biotinylated C6 or C6ΔFIM1-2 at 3 µg/mL followed by blocking with 0 or 500 nM CP010. The sensors were equilibrated in running buffer and dipped in a well containing either 100 nM native C5 alone or in the presence of 10 nM CVFBb, leading to generation of C5b. Association was monitored for 2 h, and the background (CVFBb either with CP010 bound or without) was subtracted.

Western Blot

Aliquots of C6, immunoaffinity purified using CP010 or 20D2, were separately run on SDS-PAGE under reducing and non-reducing conditions and then electrophoretically transferred onto a 0.45-µm nitrocellulose membrane (GE Healthcare). After transfer, non-specific sites on the membrane were blocked with 3% BSA in PBS containing 0.05% Tween 20 (PBS-T). After washing in PBS-T, membrane strips were incubated overnight at 4°C with CP010 or 20D2; each at 1 µg/mL in 3% BSA PBS-T. After washing, bound CP010 or 20D2 were detected by incubation with the donkey anti-mouse IgG-HRP conjugate (715-035-150; Jackson ImmunoResearch) at 1 in 10,000 dilution in 3% BSA PBS-T. After washing, the blot was developed with enhanced chemiluminescence (GE Healthcare) and visualized by autoradiography.

In vivo Testing of the Humanized 7E5 Antibody in HC6 BAC Transgenics

All animals were fed ad libitum and were housed in normal 12 h day/night cycles. HC6 transgenic rats on the SD background were generated by pronuclear injection of a BAC clone (RP11-507F11) containing the hC6 gene (Cyagen Biosciences, Jiangsu, China). Expression of hC6 from the BAC clone was tested in embryos, and expression was confirmed by both qPCR and Western blot. Several transgenic lines were made, and based on the tissue expression pattern, one line was selected for breeding. Transgenic animals were maintained at Janvier-Laboratories (Saint Berthevin Cedex, France). Rats were re-derived under SPF conditions and then backcrossed with C6-deficient PVG rats [37] for >20 generations. Integration sites were mapped using the targeted locus amplification technology (Cergentis B.V., Utrecht, the Netherlands). The 5′-integration site was mapped to rat chr18:59862683, the 3′-integration to chr18:59870270-59870290; ~7.6 kb of rat genome sequence (Rnor 5) was deleted that contains exons of the Nedd4L gene. Breeding of the transgenic rats was done by pairing a heterozygous and a C6-deficient animal, and the rats breed normally without a visible phenotype. The heterozygous breeding resulted in littermate C6-deficient and hC6-sufficient animals. The C6 sufficient animals had a normal terminal pathway activity as compared to wild-type rats as measured by a CH50 assay (*data not shown*).

For experiments with the hC6 BAC transgenics, the expression levels of hC6 was measured in all transgenic animals before allocating them to experimental groups to ensure an equal distribution of C6 expression variability in all groups. The hC6 protein levels varied between 24.8 μg/mL and 58.8 μg/mL. These levels are within normal natural range and are sufficient for full MAC activity. C6 deficiency in PVG $C6^{-/-}$ animals was confirmed before allocation to the experiment. In addition, equal numbers of both sexes were allocated to the treatment groups. Thus, we made sure that both the variation in C6 expression levels and sexes were distributed evenly over all experimental groups. Age and weight distribution was also checked for each group. The determination of the size of each animal group was based on previous knowledge on the models and the approved work plan of the experiments. The administration of test articles was blinded for the animal technicians who performed the administration and kept records of clinical scores and body weight. Animals of the different experimental groups were equally distributed over cages and housed three per cage. Treatment groups were mixed within cages to avoid cage effects. The rats were chipped (Biolog id, Bernay cedex, France) for identification.

Spinal Cord Homogenate-Induced EAE

Testing in the EAE model was done at Redoxis AB (Lund, Sweden). Disease was induced in adult 8- to 10-week-old rats by subcutaneous injection at the base of the tail of 4 mg of an emulsion consisting of syngeneic PVG rat spinal cord homogenate (SCH) emulsified in CFA (Sigma-Aldrich) on day 0. Disease was evaluated daily in a blinded fashion from day 5 until the end of the experiment according to the following criteria: 0 = healthy, 1 = tail weakness, 2 = tail paralysis, 3 = tail paralysis and mild waddle, 4 = tail paralysis and severe waddle, 5 = tail paralysis and paralysis of one limb, 6 = tail paralysis and paralysis of a pair of limbs, 7 = tetraparesis or paralysis of three limbs, and 8 = premorbid or dead. The weight was measured on day −1 and regularly during the experiment to evaluate health status.

At termination, rats were perfused with formalin (histology) or PBS (RNA isolation), and the brain, kidneys, CSF (only PBS-perfused), liver, and spinal cord were collected. Spinal cords that were harvested for histology were dissected into cervical, thoracic, and lumbar regions. Tissues from formalin-perfused animals were kept in formalin for 48 h at 4°C and then transferred to 70% ethanol until shipment. Spinal cords harvested for RNA isolation and RNA-Seq were dissected into cervical, thoracic, and lumbar regions, separately snap-frozen in liquid nitrogen or on dry ice and stored at −80°C.

Experimental Autoimmune Myasthenia Gravis

Passive EAMG was induced in rats by subcutaneous injection on day 0 with anti-acetylcholine receptor mAb35 [38] in PBS at 1 mg/kg in a total volume of 100 μL per rat. The rats were weighed daily between day −1 and end of the experiment as a measurement of general health status. A grip test was carried out measuring the strength of the forepaws. Briefly, each rat was allowed to acclimatize with the machine and was then gently placed in front of it. Forepaws were placed on the plunger, and the rat was pulled away.

Disease was evaluated twice daily in a blinded fashion according to the following criteria: 0 = healthy (normal strength, grips and lifts cage lid with forepaws); 1 = reduced grip strength in forepaws (gripes but cannot lift cage lid); 2 = loss of grip in forepaws; 3 = loss of grip in forepaws, hunched posture, hind limb weakness; 4 = loss of grip in forepaws and hind limb paralysis; 5 = moribund. Data collected from morning and afternoon scoring sessions were averaged for graphic preparation.

Efficacy of C6 Monoclonal in SCH-Induced EAE and EAMG Models

The efficacy of the 7E5 NALAPG antibody was tested in both the EAE and the EAMG models, using the MOTA NALAPG antibody as the isotype control to exclude non-specific immunoglobulin mediated effects. The minimum number of animals needed per treatment group was determined by performing pilot experiments with the hC6 BAC $C6^{-/-}$ PVG strain and the PVG $C6^{-/-}$ strain and then performing a power analysis (Power 80% Alpha 0.05) using the clinical score (see above) as a primary outcome.

In the EAE model, vehicle (PBS $n = 41$), MOTA NALAPG mAb ($n = 45$, 40 mg/kg), or 7E5 NALAPG mAb ($n = 45$, 40 mg/kg) was administered via intraperitoneal (i.p.) injection on days 15, 20, 24, and 28 after disease induction. A group of non-treated C6-deficient rats ($n = 29$) was also included. Animals reaching the humane endpoint (clinical score >6) were euthanized. Twelve females (two in the saline, three in the 7E5 NALAPG, three in the MOTA NALAPG group, and four in the C6-deficient group), and three males (one in the saline and two in the MOTA NALAPG group) were killed before the end of the experiment because they reached the humane endpoint. Most animals reaching the humane endpoint were removed until day 15 (before they were administered any test item), and therefore, the data from these rats are included in the results until the day of removal. In contrast, data from 2 rats which were sacrificed on days 21 and 22 (1 female and 1 male, both from the MOTA NALAPG group) are included in the results until the end of the experiment (carry over last measurement). Rectal temperature was measured prior to premature termination. All the remaining rats were euthanized on day 30 (end of experiment).

In the EAMG model, saline ($n = 8$) or 7E5 NALAPG mAb ($n = 8$, 40 mg/kg) was administered i.p. on day 0, in a total of 1 injection per rat. A group of non-treated C6 BAC ($n = 8$) and a group of C6-deficient ($n = 8$) rats were also included. All mice were terminated at 72 h after disease induction.

Epitope Mapping by Mass Spectrometry

C6 (3 μg) was trypsin-digested for 10 min at 37°C. The trypsin digest was run on 10% SDS-PAGE. On Western blot, a 20-kD band was detected by 7E5; the band at this size was excised from separate SDS-PAGE gels of trypsin-cleaved C6 stained with Coomassie brilliant blue. Gel slices were rinsed in pure water, cut into 1-mm3 blocks, and collected in an Eppendorf tube. Gel fragments were destained twice for 15 min in 50 mM ammonium bicarbonate and 50% (vol/vol) acetonitrile. Supernatant was removed, and gel fragments were covered with 50 μL of 10 mM DTT in 100 mM ammonium bicarbonate and incubated at 56°C for 45 min. After removing the supernatant, the gel fragments were immediately covered with 50 μL of 55 mM iodoacetamide in 100 mM ammonium bicarbonate and incubated for 30 min in the dark. After removing the supernatant, gel pieces were covered with 50 μL 100 mM ammonium bicarbonate and incubated for 5 min.

After dehydration in 100% acetonitrile and drying in a Speedvac, the gel pieces were incubated with sequencing grade trypsin (Promega; 10 μg/mL in 50 mM ammonium bicarbonate) overnight at 37°C. Peptides from the gel pieces were extracted twice with 200

μL 50% acetonitrile in 0.1% trifluoroacetic acid. The extracts were then dried in a SpeedVac and stored at −20°C until further analysis. The peptides were re-dissolved in 15 μL of 0.1% acetic acid of which 10 μL was injected into an Eksigent nano HPLC system coupled to an LTQ Orbitrap mass spectrometer (Thermo Fisher Scientific). The peptides were initially trapped on a 5-mm PepMax 100 C18 column (Dionex; 100 μm ID, 5 μm particle size). Separation was achieved using a capillary reverse-phase C18 column that had been equilibrated with 0.1% acetic acid, 94.9% H_2O, 5% acetonitrile at a flow rate of 400 nL/min. The peptides were eluted by increasing the acetonitrile concentration linearly from 5 to 40% in 80 min and to 90% in 10 min, using the same flow rate. The LTQ Orbitrap mass spectrometer was operated in a data dependent mode, in which one full-scan survey mass spectrometry (MS) experiment (m/z range 350–2,000) was followed by MS-MS experiments on the 5 most abundant ions.

Proteome Discoverer software (version 1.4.0.288; Thermo Fisher Scientific) was used for spectrum annotation. Mass spectra were annotated against the Uniprot human proteome database (release 2013-09). The search parameters were MS accuracy 10 ppm, MS-MS accuracy 0.8 Da, fixed modification of cysteine alkylation with iodoacetamide, variable modification of methionine oxidation, and protein N-terminal acetylation. Enzyme specificity was set to Trypsin/P, allowing at most two missed cleavages.

Free C6 Measurement

MSD plates (Meso Scale Diagnostics LLC, Rockville, MD, USA) were spot-coated with 7E5 NALAPG at 10 μg/mL spot. Rat serum samples were diluted 400-fold in PBST/1% Blocker A (Meso Scale Diagnostics LLC). Bound hC6 was detected with biotinylated anti-hC6 13H5 mAb (AdipoGen, San Diego, CA, USA) at 1 μg/mL combined with SA-SULFO (Meso Scale Diagnostics) present at 0.5 μg/mL. A concentration range of purified hC6 in Lewis rat serum was used for calibration curves. This assay had a detection range of 0.4–800 μg/mL.

Pathology

Histology

Formalin-fixed spinal cords from each of the three levels (cervical, thoracic, and lumbar) were embedded together in a single paraffin block (1 block/animal; maintaining levels separate from one another). For each animal, two transverse sections from each level of the spinal cord were trimmed and stained with haematoxylin and eosin (H&E) and Luxol fast blue (LFB). Images were acquired with a digital camera (Leica Microsystems BV, Rijswijk, the Netherlands) attached to a light microscope (Leica Microsystems BV) for colorimetric staining.

Microscopic Evaluation and Scoring

Terms used for microscopic evaluation were based on grading rubrics developed for EAE [39]. The histological examination was performed by Tox Path Specialists, LLC (Frederick, MD, USA) (https://www.toxpath.net/). All observers were blinded for treatment group assignment. Changes in the spinal cord were diagnosed based on their anatomic location and separated into grey or white matter. Inflammation was assessed using H&E slides. The grade for inflammation was based on the following rubric: 1 = a few scattered inflammatory cells; 2 = organization of inflammatory infiltrates into perivascular cuffs (typically more than one cell layer thick) or confluent clusters of inflammatory cells; 3 = extensive perivascular cuffing with extension into adjacent subarachnoid space and CNS parenchyma and/or infiltration of parenchyma with inflammatory cells; 4 = extensive perivascular cuffing with increasing subarachnoid and parenchymal inflammation and/or pronounced infiltration of parenchyma with inflammatory cells; 5 = inflammation extending throughout entire anatomic subsite. The grade for gliosis was based on the following criteria: 1 = barely exceeds normal limits; 2 = gliosis more readily apparent than a minimal finding, focal, or multifocal; 3 = gliosis readily apparent, focally extensive, or multifocal; 4 = gliosis pronounced affecting a prominent portion of a spinal cord region; 5 = gliosis very pronounced affecting a prominent portion of a spinal cord region. Demyelination was assessed using LFB slides. Loss of blue staining on LFB-stained slides was interpreted as demyelination. Demyelination was scored on the white matter according to the following rubric: 1 = a few scattered naked axons; 2 = small groups of naked axons; 3 = large groups of naked axons; 4 = confluent foci of demyelination; 5 = widespread demyelination.

Statistical Analysis

Statistical tests were performed using GraphPad Prism (v9.0.1; GraphPad Software). Normality of the variable distribution was assessed by the Shapiro-Wilk test. When the test distribution was not normal, a non-parametric Mann Whitney or Kruskal-Wallis test was used. When the test distribution was normal, a t test or ANOVA test was applied. Data are represented as a mean ± SEM. The results were considered significant when p value <0.05 at a 95% confidence level.

RNA Sequencing and Analysis

RNA Sequencing

Tissue was lysed in a MagNA Lyser using TriPure (Sigma-Aldrich) and MagNA Lyser green beads (Roche). RNA was isolated using QIAGEN QIAcube and quality checked with a Bioanalyzer RNA Nano Chip (Agilent). cDNA synthesis was performed using the NuGEN Ovation RNA-Seq System V2 (7102-A01; NuGEN, San Carlos, CA, USA) followed by purification with the QIAGEN MinElute Kit. cDNA was sheared to 200–400-bp fragments. The cDNA was end-polished and dA-tailed, and adaptors with Bioo barcodes were ligated (Life Technologies). The fragments were amplified (eight cycles) and quantified with a QuBit (Thermo Fisher Scientific). RNA-seq was done by Genome scan (Leiden, the Netherlands; https://www.genomescan.nl/) using a NovaSeq 6000 PE150 (Illumina).

Pathway Analysis

RNA-Seq files were processed using the open source BIOWDL RNAseq pipeline v2.0.0 developed at the LUMC. This pipeline performs FASTQ preprocessing (including quality control, quality trimming, and adaptor clipping), RNA-Seq alignment, and read quantification. FastQC (v0.11.7) was used for checking raw read QC. Adaptor clipping was performed using Cutadapt (v2.4) with default settings. RNA-Seq read alignment was performed using STAR aligner (v2.7.3a) [40]. The gene read quantification was performed using HTSeq-count (v0.9.1) [41] with setting "stranded yes." The gene annotation used for quantification was Rnor 6.0 with the human BAC sequences added. The raw counts were converted to CPM (+1) counts, and from this, fold changes were calculated for every comparison. The data were analysed using Ingenuity Pathway Analysis (QIAGEN Inc., https://www.qiagenbioinformatics.com/products/ingenuity-pathway-analysis/) [42].

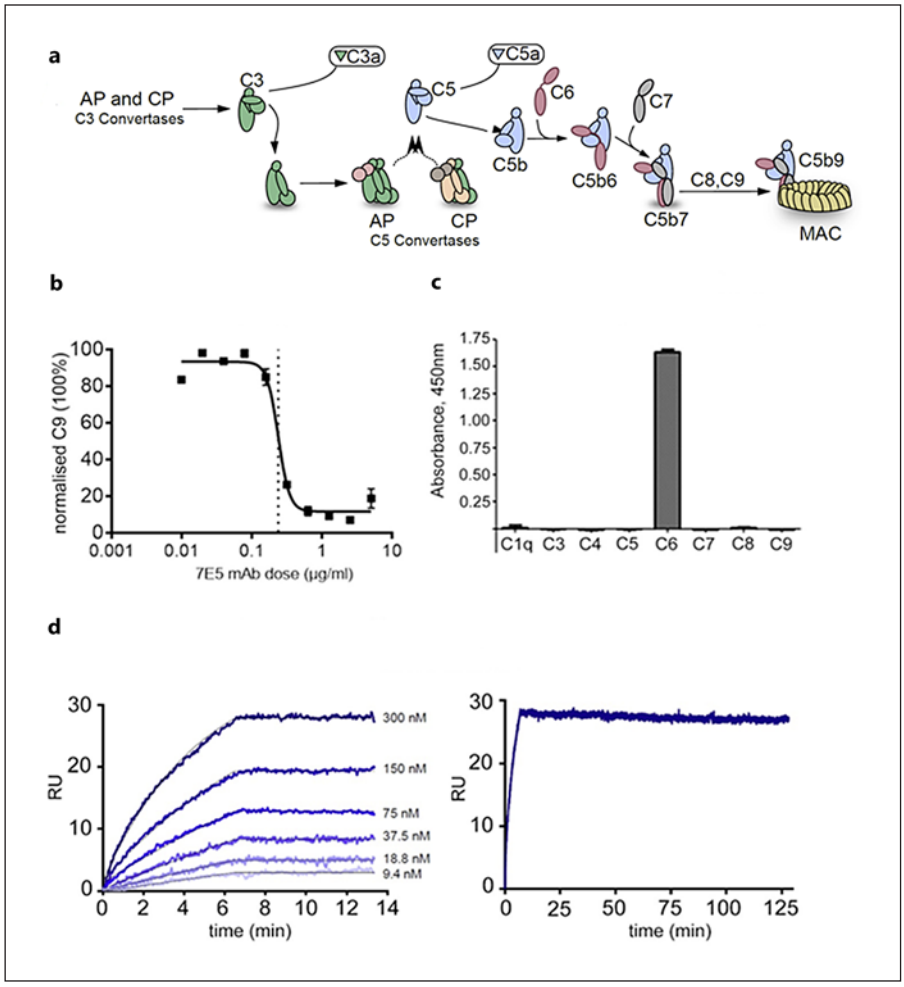

Fig. 1. Specificity and in vitro kinetics of the rat 7E5 mAb. **a** The complement system. C3a and C3b are generated by cleavage of C3 by the C3 convertases. Surface-bound C3b acts as an opsonin, whereas soluble C3a acts as an anaphylatoxin. Similarly, C5a and C5b are generated by cleavage of C5 by the C5 convertases (terminal pathway). Surface-bound C5b initiates MAC formation. Soluble C5a acts as an anaphylatoxin. **b** ELISA measuring C9 attached to the plate (MAC ELISA) showing that 7E5 is a potent inhibitor of complement-mediated lysis in the human serum. **c** ELISA showing that 7E5 binds only to hC6 and not to other complement components. **d** SPR analysis of different concentrations of analyte 7E5 binding to immobilized ligand hC6 on the sensor surface with high affinity (left). The experimental data could be fitted well with a 1:1 interaction model with values for the association constant (k_a) was 1.7×10^4 $M^{-1}s^{-1}$, the dissociation constant (k_d) was 4.3×10^{-6} s^{-1}, and the calculated K_D was 2.5×10^{-10} M. To the right is displayed the curve for the 300 nM experiment over 125 min to visualize the very slow dissociation of the antibody from immobilized C6.

Results

Isolation of a Terminal Pathway Blocking C6 Monoclonal Antibody

C6-deficient rats (PVG $C6^{-/-}$) were immunized with the hC6 protein, and hybridomas were generated using standard procedures. One clone 7E5-14E4 (IgG1) was selected based on its capacity for inhibition of complement-mediated sheep erythrocyte lysis and an ELISA-based screen for inhibition of C9/terminal complement complex (TCC) deposition. 5′-RACE was used to determine sequences of the heavy and light chains, and these were re-cloned on a rat IgG2c constant region. We refer to this rat clone as 7E5. The fully humanized version of 7E5 with a human IgG4 S228P constant region is designated CP010.

The 7E5 monoclonal antibody is an inhibitor of MAC formation in human serum in vitro (Fig. 1b). However, in some experiments, a residual activity in CH50 assays was present (online suppl. Fig. 1A). Maximum inhibition was seen in freshly harvested serum, whereas CH50 in serum stored for 24 h at ambient temperature could not be blocked completely, even at higher concentrations of the antibody. To determine the mechanism responsible for this in vitro-generated lytic activity, C6 was immunoaffinity-purified from serum using 7E5 or its humanized version CP010 and another C6 mAb, 20D2 (which binds a different epitope on C6) and used in a CH50 reconstitution assay with C6-deficient serum (online suppl. Fig. 1B). Activity of C6 isolated on CP010 was completely blocked by CP010 in this assay, whereas C6 isolated by 20D2, another C6 specific antibody, could not be inhibited completely by CP010. Western blot analysis of the 20D2-purified C6 fractions showed a slightly shorter C6 fragment on non-reduced gels detected by 20D2 but not CP010 (online suppl. Fig. 1C); the fragment was not ap-

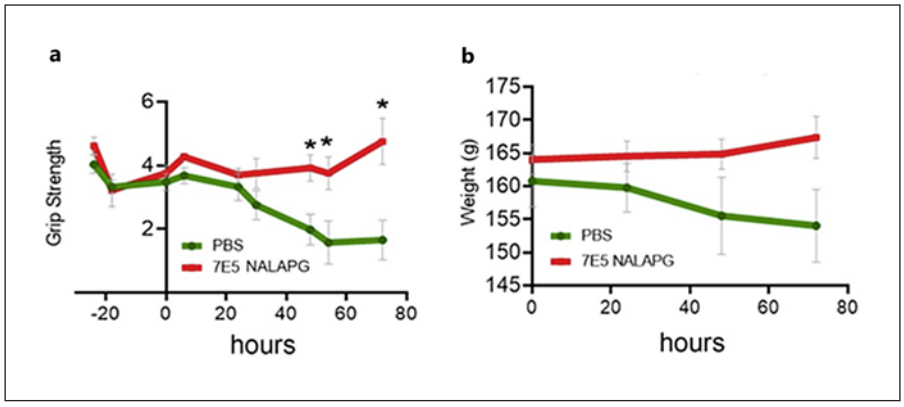

Fig. 2. Effect of C6 inhibition in EAMG. **a**, **b** EAMG was induced in humanized (h) C6 rats ($n = 10$) by subcutaneous injection of a solution containing 2 mg/kg of an antibody against acetylcholine receptor mAb35 on day 0. The rats were administered intraperitoneally with PBS (vehicle) or 7E5 NALAPG mab (40 mg/kg) on day 0, in a total of 1 injection per rat. Grip strength was measured in both front paws from day −1 (−24 and −30 h) until day 3 (72 h) post-EAMG induction and are plotted in the graph. **a** The PBS group showed a significant reduction of grip strength compared to the 7E5 NALAPG group on days 2 (48 and 54 h) and 3 (72 h). (**a**). **b** Weight was also measured on day 0, day 1 (24 h), day 2 (48 h), and day 3 (72 h) after EAMG induction. Administration of the 7E5 NALAPG showed a marginal effect on weight of the treated compared to the PBS rats on day 3 (72 h) post-disease induction (**b**). Data represent the average clinical scores (mean) ± SEM. Significant statistical differences are indicated (*$p < 0.05$).

parent in 20D2-probed westerns of C6 purified from the same serum batch on CP010. The data suggested that an in vitro cleavage fragment of C6 was generated in serum which contributed to MAC formation but was not recognized by the CP010 antibody.

ELISA showed that 7E5 was specific to hC6 and did not cross react with any other human complement component (Fig. 1c). SPR analysis revealed that the 7E5 bound strongly to immobilized hC6 with an apparent $K_D = 2.5 \times 10^{-10}$M; the K_D was primarily influenced by an extremely low dissociation rate constant (k_d 4.3×10^{-6} [s^{-1}]) which predicts robust binding of the mAb to hC6 in vivo (Fig. 1d). A classical pathway activation ELISA was used to evaluate cross-species specificity. The 7E5 mAb prevented terminal pathway activation and C9/TCC deposition in the serum from marmoset or cynomolgus monkeys at similar dilutions to those used for human serum (online suppl. Fig. 2A, B). In contrast, the 7E5 mAb showed does not detect C6 in rat serum, and no significant effect on MAC formation assays was seen in rodent sera. Overall, these data showed that 7E5 binds human and primate C6 with high affinity and acts as a potent inhibitor of MAC assembly.

7E5 Treatment Inhibits Disease Course in EAMG and Relapsing EAE in vivo

To study the in vivo efficacy of 7E5, we tested whether systemic administration of a C6 antibody could modulate the phenotype in an acute myasthenia model (EAMG) and crEAE. For the in vivo experiments, we modified the 7E5 mAb within the hIG1-Fc domain (hIgG1-P329G NALA; 7E5 NALAPG) to abolish Fcγ receptor interactions and prevent complement activation [29]. An isotype control antibody (motavizumab, MOTA) [43] similarly modified to prevent immune effector functions was used to exclude an antibody related effect on disease progression.

Since 7E5 NALAPG is specific to hC6, we used the PVG rat strain deficient for rat C6 and transgenic for the hC6 BAC, here referred to as humanized (h)C6 rats. Myasthenia was induced by subcutaneous injection of the antibody Mab35 directed to the acetylcholine receptor [44, 45]. A comparison of C6 transgenic PVG rats with C6-deficient PVG rats demonstrated a clear dependence of disease induction on C6 (online suppl. Fig. 3). While C6 transgenic PVG rapidly developed progressive weight loss and weakness, scored as described in Methods, C6-deficient PVG rats did not. Treatment of C6 transgenic PVG with a single dose of 7E5 at 40 mg/kg on day 1 completely prevented the progressive weakness (Fig. 2a) and weight loss (Fig. 2b) in the model [45]. This shows that systemic administration of 7E5 blocks C6 activity in vivo and prevents MAC-induced injury.

Next, we tested whether systemic administration of 7E5 can affect progression of CNS disease. We previously showed that C6 inhibition after the disease onset using

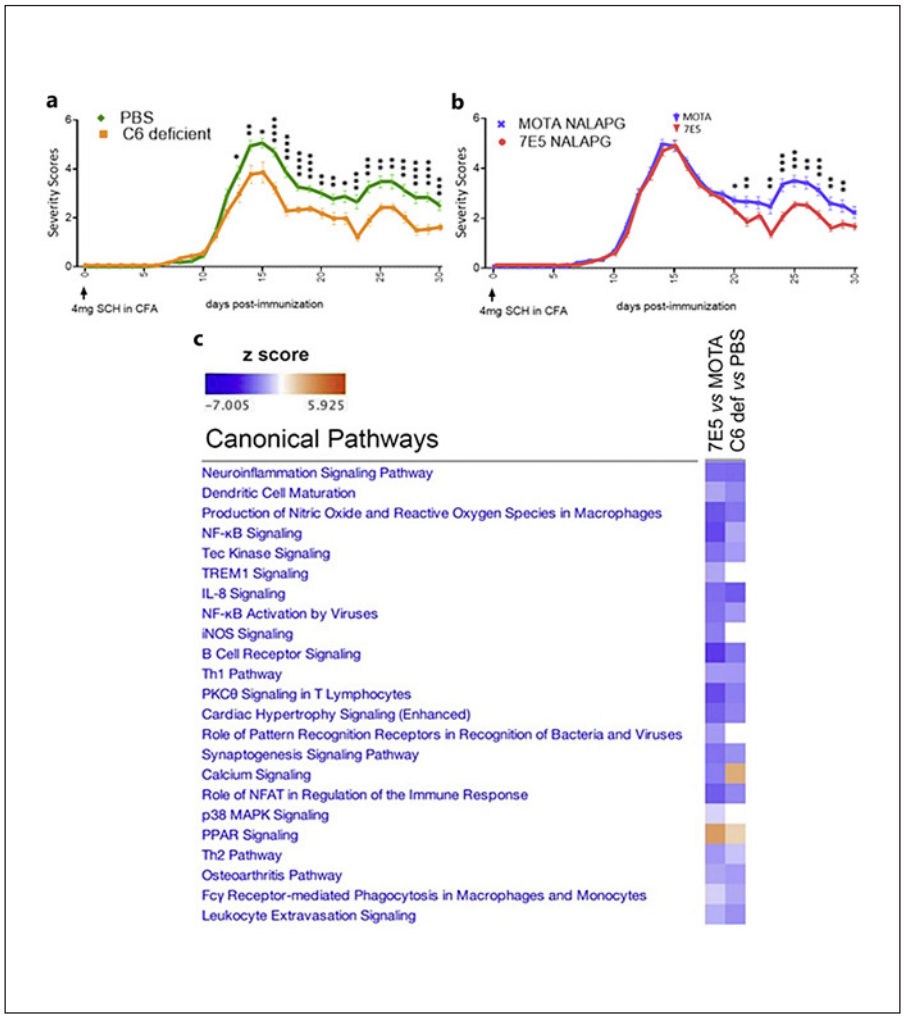

Fig. 3. C6 inhibition at peak of disease mitigates severity at relapse. **a**, **b** crEAE was induced in humanized (h)C6 rats by subcutaneous injection on day 0 of an emulsion containing 4 mg SCH. The rats were administered i.p. with PBS or MOTA NALAPG control mAb (40 mg/kg) or 7E5 NALAPG mAb (40 mg/kg) on study days 15, 20, 24 and 28. Clinical scores of rats receiving PBS ($n = 41$, in green) or rats deficient for C6 (negative control, $n = 29$, in orange) are plotted in graph **a**. Clinical scores of rats receiving MOTA NALAPG (isotype control antibody against an antigen absent from rats served as positive control, $n = 45$, in blue) or 7E5 NALAPG ($n = 45$, in red) are plotted in the graph **b**. The 7E5 NALAPG group showed a ameliorated relapse (from day 24 until day 30) compared with the MOTA NALAPG group (**b**). Data represent the average clinical scores (mean) ± SEM. Statistical differences are indicated (*$p < 0.05$, **$p < 0.01$, ***$p < 0.001$, ****$p < 0.0001$). **c** Heatmap showing IPA of canonical pathways after analyses of gene expression data from spinal cords of rats with crEAE collected at relapse (day 30). The heatmap shows that 7E5 NALAPG prevents activation of key immune pathways compared with the MOTA NALAPG isotype control antibody, an effect also seen in the C6-deficient rats when compared with PBS rats. Pathways are ranked according to the *z*-score that predicts activation (orange) or /suppression (blue). IPA, Ingenuity Pathway Analysis.

antisense oligonucleotides reduced disease severity in crEAE in Biozzi mice [17]. An effect of systemic anti-C6 administration on a CNS disease would suggest that the majority, if not all, complement C6 in the brain is produced in the periphery, mainly the liver (GTExPortal, Gencode ID: ENSG00000039537.13) [46]). Since we were limited to targeting hC6, we used our (h)C6 rats instead of mice. crEAE was induced in hC6 rats by a single injection of syngeneic SCH emulsified with CFA. To test the therapeutic effect of 7E5 NALAPG to limit disease relapse, we started treatment with 40 mg/kg of the antibody intraperitoneally just after the peak of acute disease (day 15, Fig. 3) and every 4th day thereafter. Since a high dose of the non-specific antibody (IvIg) can mitigate neuroinflammation, we included the MOTA isotype control antibody and compared the effect of 7E5 NALAPG on clinical scores and spinal cord gene expression and pathology of sick rats to the effect of the control antibody MOTA NALAPG (40 mg/kg) or saline (PBS) or to C6 deficiency.

The C6-deficient animals developed a milder acute phase of disease and showed a reduced severity of relapse compared to hC6-expressing animals, suggesting a role of the terminal pathway in acute disease and relapse. The hC6-expressing 7E5 NALAPG-treated group ($n = 45$) also showed a mitigated relapse, mirroring that in the C6-deficient animals, whereas the relapse was not affected in hC6-expressing MOTA NALAPG-treated rats ($n = 45$), equivalent to that observed in the PBS group ($n = 41$, Fig. 3a, b).

To understand the mechanisms responsible for the 7E5 NALAPG-mediated effects on disease relapse, we analysed the RNA expression profiles of spinal cords obtained at relapse (day 30 p.i.) from sick 7E5 NALAPG-

treated (n = 5), MOTA NALAPG-treated (n = 6), C6-deficient (n = 3), and PBS (n = 6) rats and performed pathway analysis using Ingenuity Pathway Analysis [42]. Focussing on canonical pathways, we found that key pathways of neuroinflammation were downregulated (coloured blue, z-score <0) or not altered (blank, z-score = 0) in the sick 7E5 NALAPG-treated rats when compared to the sick MOTA NALAPG-treated rats, as well as in the sick C6-deficient rats when compared to the sick PBS-treated rats (Fig. 3c).

To further evaluate the efficacy of 7E5 NALAPG in crEAE, we studied spinal cords collected at relapse (day 30 p.i.) from sick 7E5 NALAPG-treated (n = 13), MOTA NALAPG-treated (n = 12), and PBS (n = 11) rats. Changes in the spinal cord were diagnosed based on their anatomic location (cervical, thoracic, lumbar) separated into grey or white matter. Demyelination was assessed using LFB slides; gliosis and inflammation were assessed using H&E slides. The grading for demyelination, gliosis, and inflammation was based on previously published rubrics [39] briefly described in the Methods.

Changes associated with disease were prominent in the white matter areas of the entire spinal cord (cervical, thoracic, and lumbar segments, Fig. 4a) unlike the grey matter, where changes were subtle (*data not shown*). Differences between the groups were significant at the cervical and thoracic levels but marginal at the lumbar level (Fig. 4b). More specifically, at the cervical level, demyelination was significantly reduced in the 7E5 NALAPG rats compared to the PBS rats (**$p < 0.01$). In addition, at the cervical level, the 7E5 NALAPG rats showed significantly less gliosis compared to the PBS (**$p < 0.01$) and the MOTA NALAPG (*$p < 0.05$) rats (Fig. 4b). Representative images from cervical spinal cord sections stained with LFB (Fig. 4e, g) or H&E (Fig. 4f, h) show the relevant histopathological differences between the 7E5 NALAPG and the MOTA NALAPG groups. At the thoracic level, demyelination (***$p < 0.001$), gliosis (*$p < 0.05$), and inflammation (*$p < 0.05$) were all significantly reduced in the 7E5 NALAPG rats compared to the MOTA NALAPG rats (Fig. 4b). At the lumbar level, demyelination was marginally reduced in the 7E5 NALAPG rats compared to the MOTA NALAPG rats ($p = 0.06$) and inflammation was also marginally reduced in the 7E5 NALAPG rats compared to the PBS ($p = 0.06$) and the MOTA NALAPG ($p = 0.06$) groups (Fig. 4b). In addition, we assigned inflammation grades to the leptomeninges. Overall assessment of meningeal inflammation at each level of the spinal cord demonstrated that the 7E5 NALAPG rats showed less inflammation compared to the MOTA NALAPG (*$p < 0.05$) and the PBS (**$p < 0.01$) rats (Fig. 4c). An estimation of the percentage of the inflammatory cell population composed of different cell types was based on an overall assessment of the inflammatory infiltrates within the leptomeninges and the parenchyma at each level. Inflammatory cells within the meninges and the parenchyma were typically mononuclear cells consistent with lymphocytes and/or macrophages (Fig. 4d).

To understand the mode of action of the systemically administered 7E5 NALAPG, we developed assays for total and free hC6 in serum. Healthy hC6 rats were injected i.p. with a single escalating dose (10, 20, 40 mg/kg) of the mAb (Fig. 5a). Prolonged dosing at 40 mg/kg every 6th day for 36 days showed accumulation of total C6 as measured by MS (Fig. 5b) and complete depletion of free C6 as measured by a free C6-specific immunoassay (Fig. 5c). Overall, these data show that systemic administration of the 7E5 NALAPG mAb leads to complete depletion of free C6 and inhibition of MAC activity in the circulation, which mitigates relapse-related disease in the crEAE model.

Binding Epitope of the C6 Monoclonal Antibody

To map the epitope of the anti-hC6 antibody 7E5, hC6 was trypsin-digested and fragments detected by 7E5 on Western blot, were gel-purified, further digested, and subjected to MS. The most abundant peptides were mapped to the two C-terminal FIM domains in C6 (residues 766–934).

To determine in detail the paratope in CP010 and epitope in C6, we prepared truncated C6 variants and investigated their ability to form complexes with full-length CP010 (Fig. 6). Reconstituted C6:CP010, C6ΔFIM1-2:CP010, and FIM1-2:CP010 complexes were subjected to size-exclusion chromatography. As expected, recombinant full-length C6 formed a stable 2:1 complex with CP010 (Fig. 6a), while the antibody was unable to bind to the truncated C6ΔFIM1-2 (Fig. 6c). Importantly, the C6 fragment FIM1-2 encompassing residues 766–934 gave rise to a well-defined complex in SEC (Fig. 6b), independent of the position of the His-tag. The data confirm that the CP010 epitope is in the FIM1-2 region.

To study the interaction between the CP010 antibody and C6 by BLI and X-ray crystallography, we prepared Fab fragments from the CP010 antibody by papain cleavage followed by partial reduction of $F(ab)_2$ to yield monomeric Fab molecules. We measured the affinity of the CP010 Fab fragment to full-length C6 and FIM1-2 by BLI and found K_D values of 0.3 nM and 2.8 nM, respectively (Fig. 6d, e; online suppl. Table 2), confirming the apparent K_D value of 0.2 nM for the C6-7E5 interaction observed by SPR (Fig. 1d).

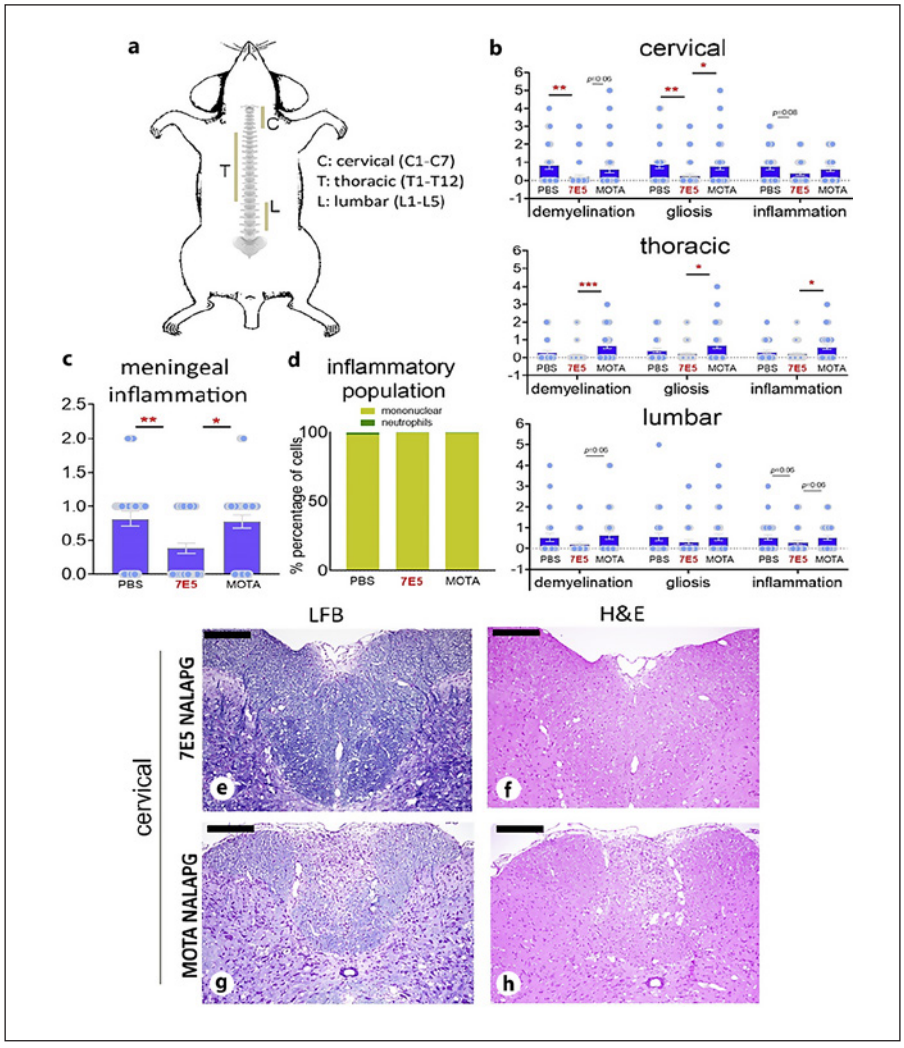

Fig. 4. 7E5 NALAPG ameliorates relapse-related spinal cord pathology. **a** Mouse cervical, thoracic and lumbar spinal cord regions. The cervical region consists of 7 vertebrae abbreviated C1 through C7 (top to bottom). The thoracic region consists of 12 vertebrae abbreviated T1 (smallest) through T12 (biggest). The lumbar region consists of 5 vertebrae abbreviated L1 (smallest) through L5 (biggest). **b** Graphs of severity scores for demyelination, gliosis and inflammation after examination of spinal cords collected at relapse (end of the experiment, day 30). Analysis was performed at the cervical, thoracic, and lumbar level of each spinal cord. Administration of the 7E5 NALAPG mab significantly reduced the average severity of demyelination, gliosis and/or inflammation at the cervical and thoracic segments in comparison with the PBS and/or MOTA NALAPG-treated rats. Data represent the average scores (mean) ± SEM. Differences between groups were analysed by using the Kruskal-Wallis test by ranks and differences are indicated (*$p < 0.05$, **$p < 0.01$, ***$p < 0.001$). **c** Graph of severity scores for inflammation in the leptomeninges. Overall assessment of inflammation in the leptomeninges at the cervical, thoracic and lumbar segments showed reduced severity in the 7E5 NALAPG compared to the PBS (**$p < 0.01$) and the MOTA NALAPG (*$p < 0.05$) rats. **d** Overall assessment of the inflammatory infiltrates within the leptomeninges and the parenchyma at the cervical, thoracic and lumbar segments showing a dominating mononuclear cells' presence. **e–h** Representative photomicrographs of sections from the cervical segment of spinal cord, stained for LFB (**e**, **g**, LFB) or haematoxylin and eosin (**f**, **h**, H&E), demonstrating the histopathology of a 7E5 NALAPG-treated and a MOTA-treated NALAPG rat. Scale bars, 200 μm.

We next crystallized the CP010 Fab:FIM1-2 complex in the presence of an anti-κ Fab-binding nanobody previously shown to promote crystallization of antigen-Fab complexes [47]. We collected X-ray diffraction data extending to a maximum resolution of 2.3 Å and solved the structure by molecular replacement (Fig. 7a). Iterative manual rebuilding and refinement generated a model with an R_{free} of 22.5% and excellent overall geometry (on-

line suppl. Table 3). The structure of the two FIM domains when bound to CP010 does not differ significantly from the structure of these domains in prior C6 and C5b6 structures, albeit the flexibility conferred by the helix connecting the two FIM domains (residues 841–857, named IFIM here, Fig. 7a) induces a slight tilt of FIM1 relative to FIM2 upon binding to CP010.

From the structure, it is evident that CP010 recognizes almost exclusively FIM2 (Fig. 7). The data support the conclusion that the hemolyticaly active proteolytic fragment found in serum is C6 missing one or both of the FIM domains (online suppl. Fig. 1). No contacts are present between CP010 and FIM1, and there is only one water-mediated interaction bridging FIM2 Arg841 with VL Asp32 (Fig. 7d) and a few van der Waals interactions to the IFIM helix. The interface between FIM1-2 and CP010 Fab buries a notable 2,317 $Å^2$ of surface area. The VL contribution is slightly smaller than the VH contribution with 1,180 $Å^2$ versus 1,327 $Å^2$, respectively. CP010 recognizes FIM2 and IFIM primarily via polar interactions, some of which are mediated by water molecules (Fig. 7b–d). This mode of interaction is reflected in the remarkable charge complementarity between the two interacting molecules (online suppl. Fig. 4), where FIM2 exhibits a large positively charged epitope surface matching well the highly negative surface on the CP010 paratope buried in the interface.

The epitope on FIM2 recognized by the antibody is formed partly by a 3_{10} helix that is bound in the groove between the VL and VH domains of CP010 and partly by β-strands 3, 4, and 6 of FIM2 (Fig. 7). In addition, several water molecules are found in the interface and support antigen binding (Fig. 7b–d). On CP010, all CDRs contribute to recognition of the antigen. VH CDR1 and CDR2 engage primarily in polar interactions with C6 (Fig. 7b). In CDR1, the backbone of Asp31 forms a hydrogen bond with the backbone of K890 in FIM2, while the Tyr33 side chain binds to the side chain of Glu913. Tyr33 also interacts with Pro886 from FIM2, both through aromatic stacking and through coordination of a water molecule mediated by their main chains. In the VH CDR2, Ser56 and Ser57 engage in hydrogens bonds with Lys907 of FIM2, and Tyr53 interacts through hydrogen bonds with both Asn910 and the backbone of Cys888. Furthermore, Asn52 coordinates a water molecule bridging to FIM2 Glu913. VH CDR3 and VL CDR2 recognize FIM2 by a combination of polar and hydrophobic interactions (Fig. 7). In VH CDR3, the backbone of Thr101 and Glu102 coordinate a water molecule, which in turn positions a neighbouring water molecule for interaction with Gln887 from FIM2 and Tyr39 from VL CDR1, respectively.

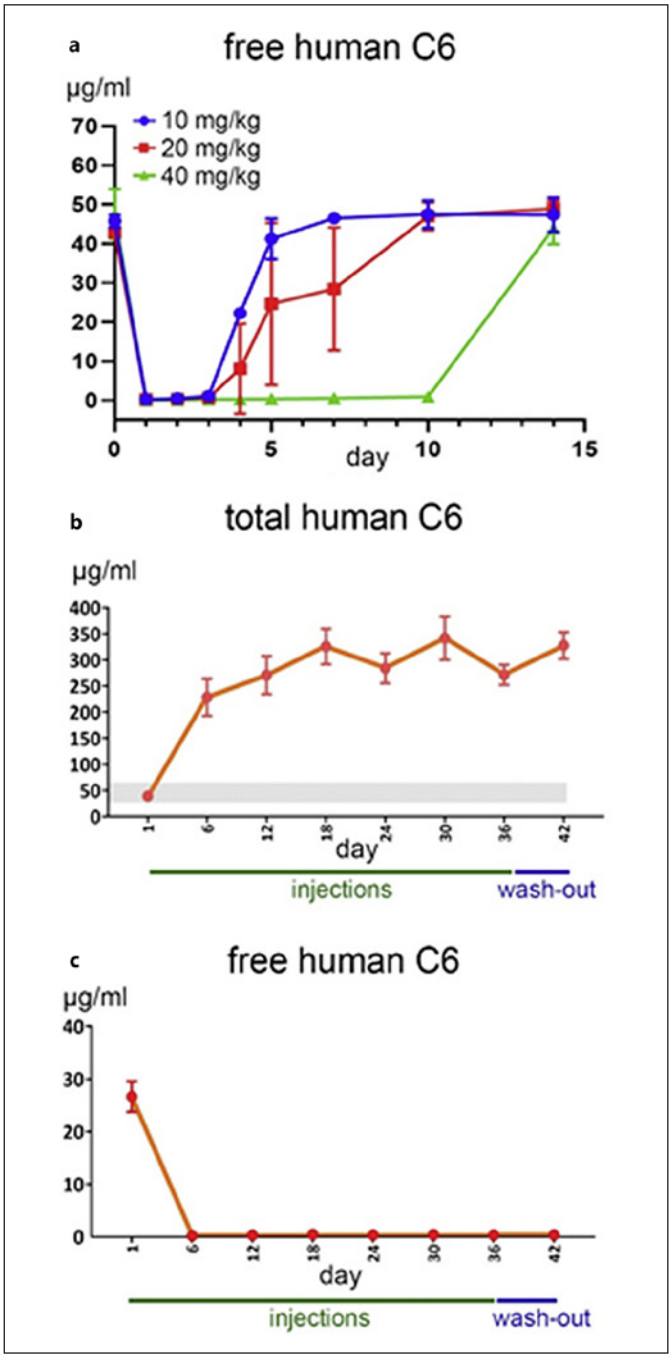

Fig. 5. Effect of 7E5 NALAPG on C6 and MAC activity levels in circulation. hC6 rats were used to model the in vivo kinetics of the 7E5 NALAPG mAb. The antibody was administered by i.p. injection. **a** Free C6 levels in a single escalating dose (10, 20, 40 mg/kg) experiment. For each dose, 2 rats were injected. **b**, **c** To assess total hC6 (**b**, bound to 7E5 NALAPG) and free hC6 (**c**), the 7E5 NALAPG mAb was injected on the following study days: 1, 6, 12, 18, 24, 30, 36. Average levels of hC6 in the non-treated female hC6 rats vary between 25 and 60 µg/mL (grey area in **b**). Free hC6, as assessed by a specific immunoassay, showed quick systemic depletion after injection with the 7E5 NALAPG mAb (**c**).

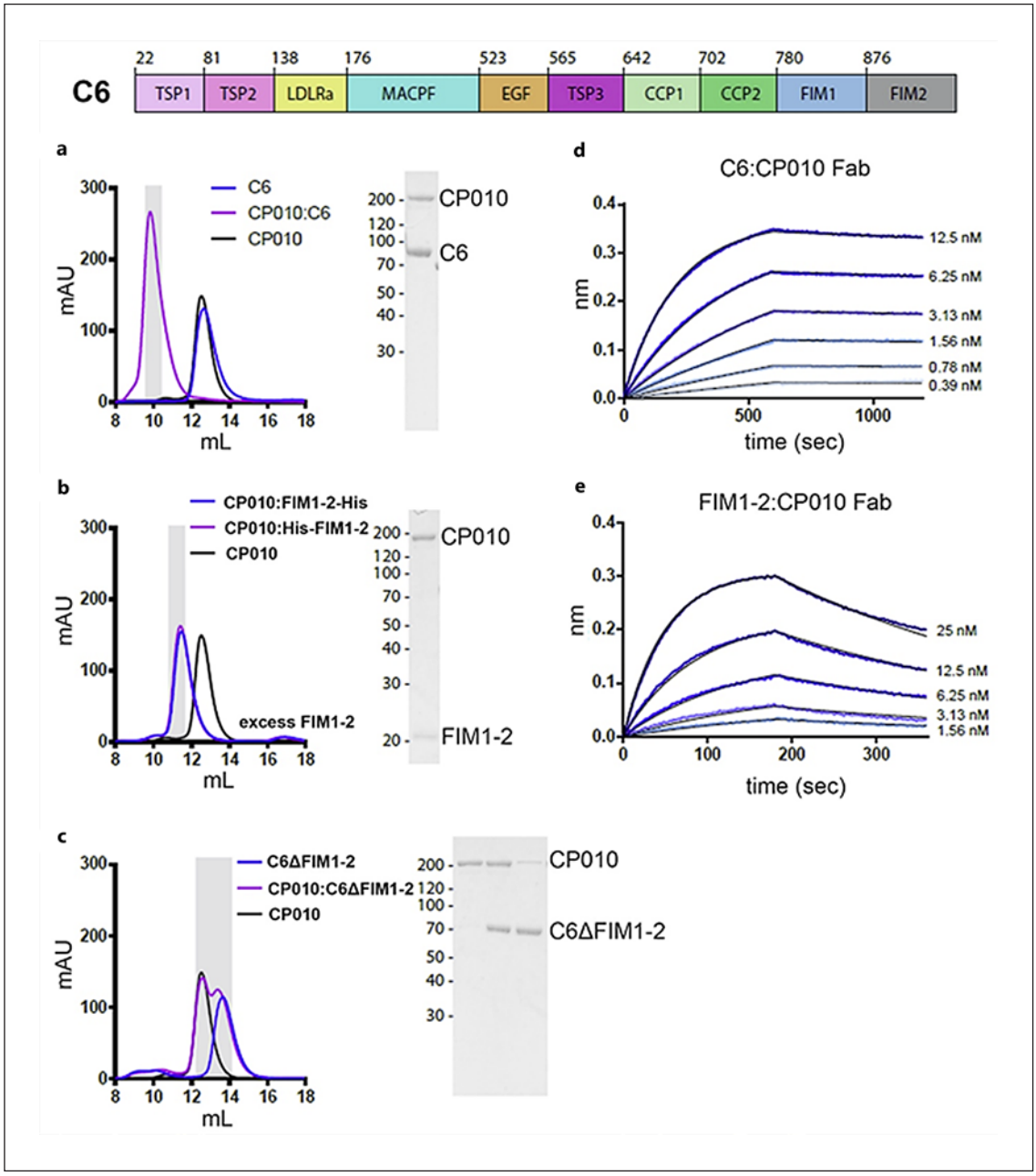

Fig. 6. CP010 (the humanized version of 7E5) binds with high affinity to the FIM domains of C6. Domain organization of complement C6 (Uniprot numbering, domain start annotated). **a–c** Size exclusion chromatography profiles of C6 variants bound to CP010, confirming binding of CP010 to the FIM1-2 domains of C6. **d**, **e** Representative BLI sensorgrams for the interaction between CP010 Fab in solution and immobilized C6 (streptavidin-coated sensors with biotinylated C6) or the FIM1-2 fragment (PentaHis sensors with His-tagged FIM1-2). Dissociation constant K_D values derived from the experiments are presented in online supplementary Table 2.

Thr101 also forms a hydrogen bond to Lys872. In VL CDR2, Asp58 engage in hydrogen bonding with Ser874 and Ser876 from FIM2, while Ser874 also binds to Ser57. Tyr54 is contacted by yet another water molecule forming a bridge to Cys873 from FIM2. VL CDR1 is an exceptionally long loop of 17 residues [48] and is engaged in numerous important interactions (Fig. 7d). Residues Asn31, Asn35, and Tyr37 coordinate a water molecule, thereby

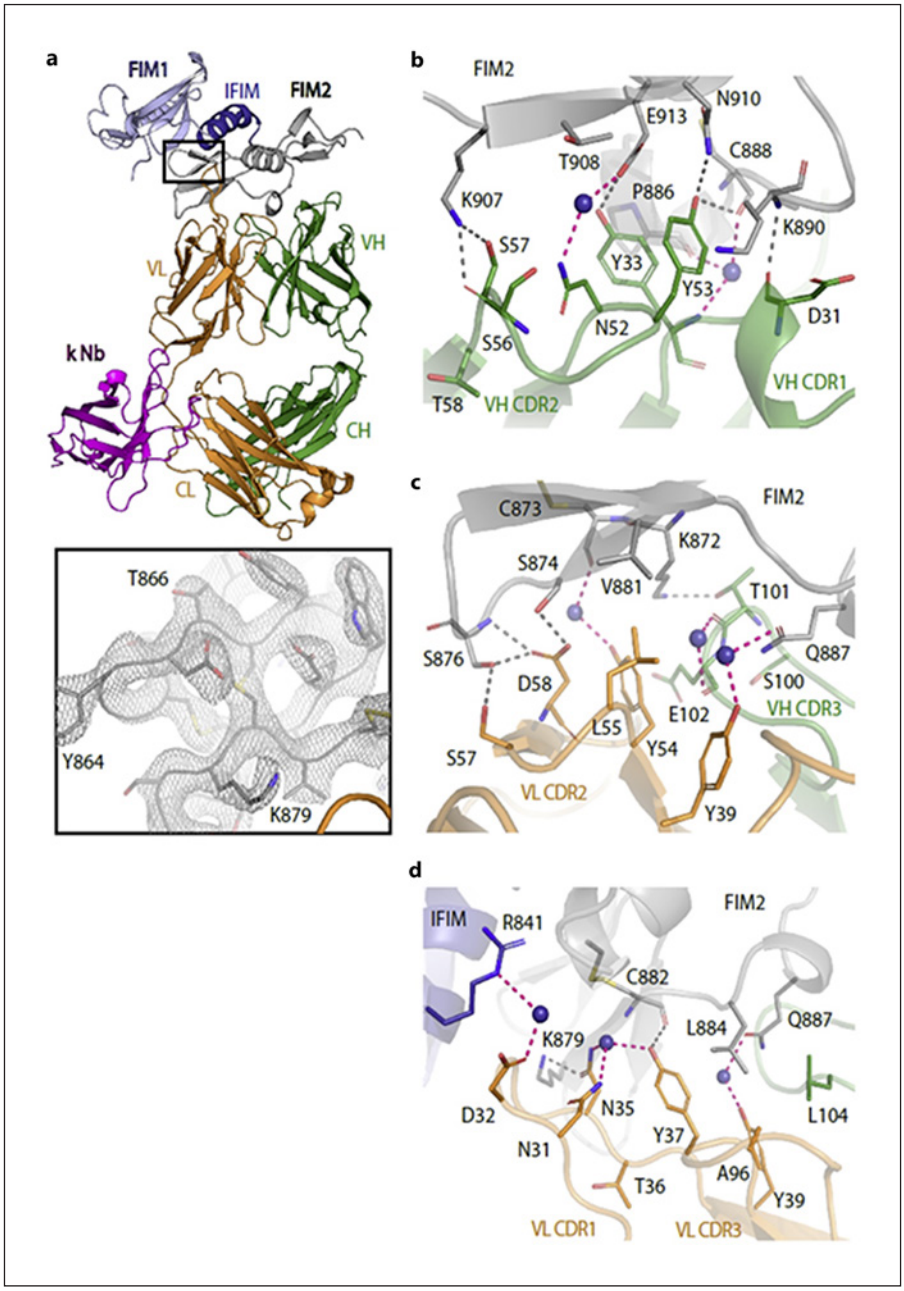

Fig. 7. The crystal structure of the CP010 Fab bound to C6 FIM1-2. **a** Cartoon representation of the complex. The Fab light chain is coloured orange, while the heavy chain is green. The κ-binding nanobody used to promote structure determination is displayed in purple. The domains of FIM1-2 are coloured in light blue (FIM1), dark blue (linker between domains, denoted IFIM), and grey (FIM2). **Inset**: Omit $2mF_o$-DF_c electron density map contoured at 1σ around residues in the FIM2 domain. The entire FIM2 (residues 858–934) was omitted for map calculation. **b–d** The interface between FIM1-2 and CP010 Fab with selected residues shown in sticks. VH CDR1 and CDR2 contacts (**b**), VH CDR2 and VL CDR1 contacts with VH CDR 3 in the back (**c**), VL CDR2 and CDR3 contacts (**d**). Hydrogen bonds are shown as grey dashed lines, while interactions mediated by water (blue spheres) are indicated by pink dashed lines.

positioning the Tyr37 side chain for interaction with the main chain of FIM2 Cys882, and Asn35 for interaction with Lys879. VL CDR3 is part of a hydrophobic milieu maintained by Ala96 and Tyr101 packing against Leu104 from VH CDR3 (Fig. 7d). Indeed, VL CDR3 together with other heavy chain (Tyr33, Pro99) and light chain (Tyr37 and Leu55) residues create a hydrophobic binding pocket that provides a docking site for the 3_{10} helix (residues 883–887) of FIM2 (Fig. 7b, d).

Identification of the CP010-binding epitope on FIM1-2 allowed us to investigate potential cross-reactivity with other species, which could be important for future clinical development. Based on the comparison of our structure of the Fab:FIM1-2 complex with a sequence alignment of the C6 FIM domains, we predicted that C6 from the dog, pig, and macaca would bind the CP010 antibody (online suppl. Fig. 5A). We prepared the corresponding recombinant FIM1-2 fragments and tested binding to CP010

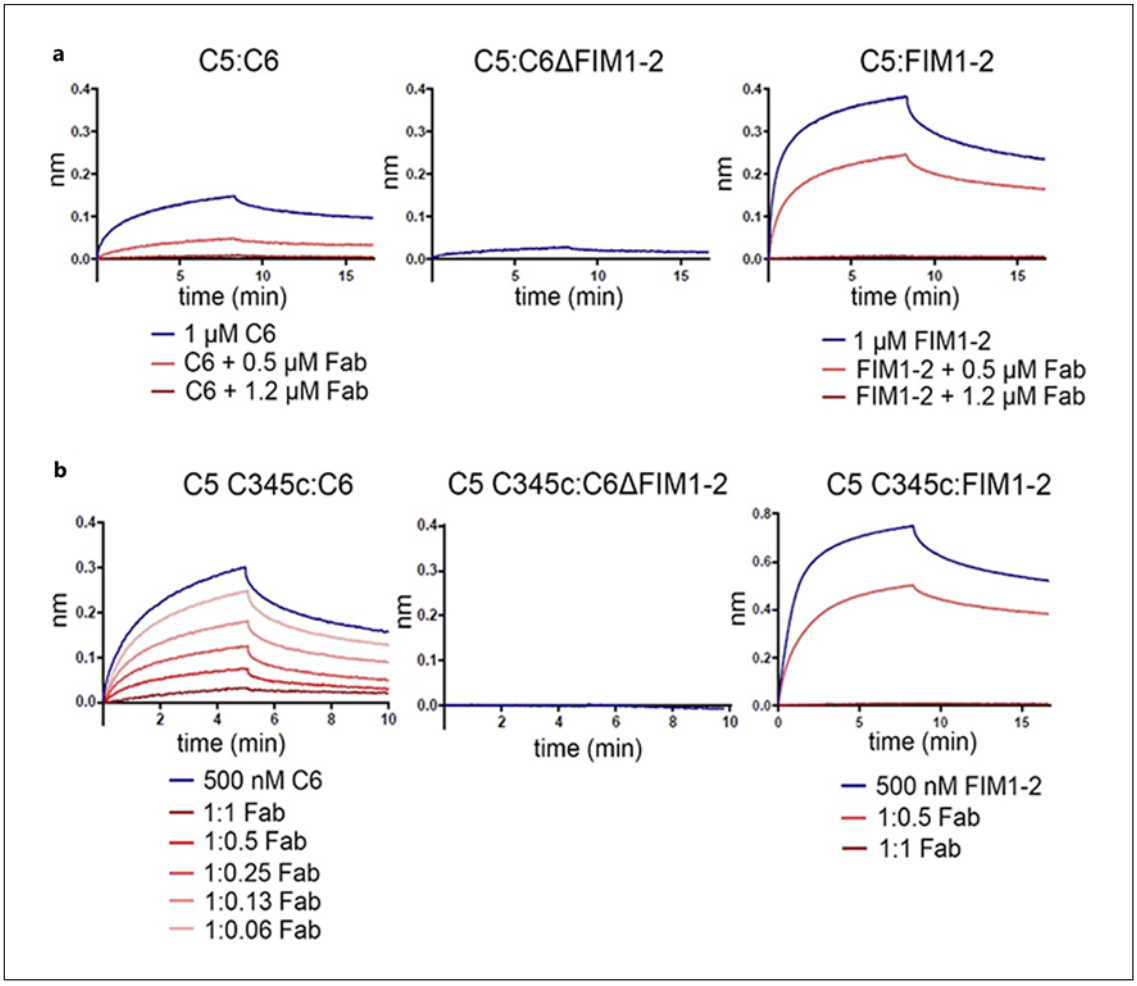

Fig. 8. CP010 prevents C6 binding to native C5 through the C6 FIM1-2 and the C5 C345c domains. **a** BLI sensorgrams demonstrating binding of 1 μM C6 and FIM1-2 but not 1 μM C6ΔFIM to native C5-coated sensors prepared by amine coupling (blue curves). CP010 Fab inhibits the interaction binding in a concentration-dependent manner (orange/red curves). **b** As in panel **a** but with the immobilized recombinant C5 C345c domain on the sensors and 500 nM of the C6 variants in solution. The red/orange/pink curves were recorded in the presence CP010 Fab, while the blue curves are from experiments without the CP010 Fab. Experiments were repeated thrice.

Fab via BLI. All species showed comparable binding affinities to human FIM1-2 of approximately 5 nM, confirming the predicted cross-reactivity (online suppl. Fig. 5B; online suppl. Table 2). These experiments with FIM1-2 fragments of non-hC6 also indirectly validated the physiological relevance of the crystal structure. A comparison of the structure and sequence alignment suggests that the lack of reactivity with rodent C6 is due to the substitutions Glu913Thr (glutamate in man, threonine in rodents), Lys879Asn, Ser876His (Fig. 7b–d and online suppl. Fig. 5A).

CP010 Anti-C6 Interferes with C5/C5b Contacts

The major interaction site for C6 onto C5b located on the C5d domain is buried in native C5 but becomes accessible following cleavage by a C5 convertase [49, 50]. However, the two FIM domains of C6 were earlier reported to bind reversibly also to the C345c domain of native C5, thereby promoting association of C5 and C6 and facilitating formation of the stable C5b6 complex [51, 52]. To investigate the mechanism of action of CP010 in complement inhibition and to reproduce these earlier results with highly purified proteins, we conducted an array of BLI experiments (Fig. 8). We first demonstrated a direct,

albeit weak, interaction between full-length C6 and immobilized native C5, while C6ΔFIM1-2 showed a strongly diminished binding to C5 (Fig. 8a), confirming earlier results [51–53]. The CP010 Fab could directly block this interaction in a concentration-dependent manner (Fig. 8a). Similarly, the C6 FIM1-2 fragment readily bound to immobilized C5, and this interaction was also completely inhibited by CP010 (Fig. 8a).

A structure describing the interface between the FIM1-2 and the C5 C345c domains remains to be determined experimentally; however, two independent crystal structures of the C5b6 complex revealed a likely model through analysis of crystal packing (online suppl. Fig. 4B) [49, 50]. Here, C5b C345c from one C5b6 complex interacts with the C6 FIM domains of a second C5b6 complex, and it was proposed that this interaction mirrors an in vivo relevant C5-C6 interface. Interestingly, the binding site for C5 C345c onto the IFIM and FIM2 overlaps partially with the binding site for CP010 (online suppl. Fig. 4B). To test experimentally if CP010 prevents the interaction, we prepared recombinant C5 C345c and tested binding to C6 in the presence and absence of the CP010 Fab (Fig. 8b). C5 C345c bound full-length C6 with an apparent K_D of 10–20 nM (online suppl. Table 2) and CP010 inhibited this interaction in a concentration dependent manner. As expected, C6ΔFIM1-2 did not interact with the C5 C345c. Lastly, the direct interaction between FIM1-2 and C5 C345c was quantitated and observed to have K_D = 5 nM; CP010 Fab blocked the interaction completely (Fig. 8b). In summary, CP010 prevents the reversible binding of C6 to native C5 by blocking interaction with the C5/C5b C345c domain.

We next set out to investigate the role of CP010, and thus the C6 FIM domains, in formation of the MAC initiator complex, C5b6 via BLI (Fig. 9). This approach demonstrated that the FIM1-2 domains strongly contribute to the association of C5b with C6 since the curves for C5b binding to C6ΔFIM1-2 and C6+CP010 are highly similar (Fig. 9b). However, C5b is still able to associate with C6ΔFIM and C6+CP010, although much less efficiently. Overall, these biophysical data demonstrated that the FIM1-2:C345c axis is important, but not absolutely required, for MAC assembly and subsequent cell lysis, confirming earlier results [52].

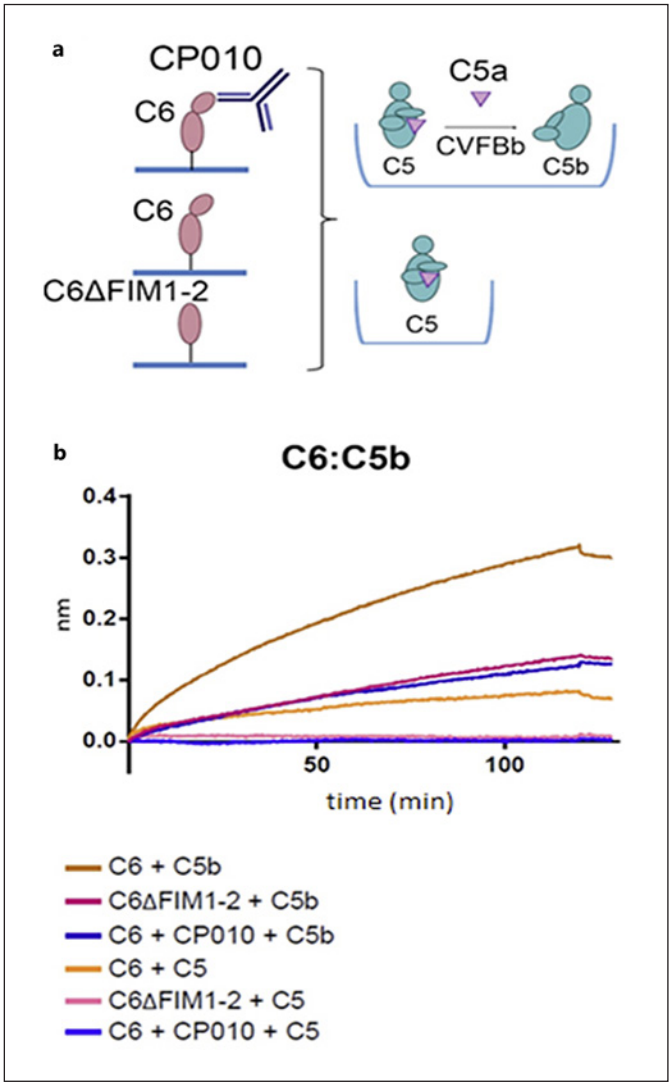

Fig. 9. CP010 inhibits the first step of MAC assembly. Investigation of C6 binding to C5b in real time using BLI. **a** Illustration of the experimental setup. Biotinylated C6 and C6ΔFIM on streptavidin sensors were either blocked by CP010 or left untreated. The sensors were subsequently dipped in a solution containing 100 nM native C5 in the presence or absence of 10 nM pre-assembled C5 convertase (CVFBb), leading to generation of C5b. The assay was continued for 2 h. The background (CVFBb for either CP010 bound or without) was subtracted. **b** Results of the assay directly showing that the FIM1-2 domains strongly contribute to the association of C5b with C6 since the curves for C5b binding to C6ΔFIM and C6+CP010 Fab are highly similar.

Discussion

Complement is an important driver of disease progression in neurodegenerative diseases. Previous studies indicate that activation of the innate immune response, especially the terminal pathway of the complement system, is critically responsible for neuronal damage. Even sub-lytic quantities of MAC directly activate the NLRP3 inflammasome causing production of IL-1β, thus driving inflammation [6, 7]. We previously demonstrated that

MAC inhibition by antisense-mediated C6 inhibition prevents activation of IL-1β formation, limits influx of macrophages, and stops neuroinflammation in the Biozzi chronic relapsing model of MS in rodents (crEAE); relapses were completely prevented even after the onset of disease [17].

The first indication that dysregulation of the complement pathway was associated with common neurological disorders came from the GWAS study on age-related macular degeneration which identified a functional sequence variant in complement factor H as a significant risk factor (OR = 7.4) [54]. Subsequent GWAS studies showed associations of sequence variants in or near complement regulators genes with susceptibility for the neurodegenerative disease Alzheimer's disease [55, 56].

The fact that association with variants in or near complement regulators is identified suggests that dysregulation of complement activation is a driver of disease progression and opens new ways for treating by blocking inappropriate complement activation. However, a reason for not implementing complement pathway inhibition in chronic disorders is the essential role of the innate immune system as a first line of defence against infections. Inhibition of the terminal pathway may be lower risk because most of the anti-infection activities of complement are upstream and deficiency in components of the terminal pathway was shown to be compatible with normal life expectancy [57].

In this study, we presented the development and characterization of a therapeutic monoclonal C6-binding antibody that prevents MAC formation. Here, we show that systemic administration of a mAb targeting C6 can reduce disease severity in two animal models; anti-acetylcholine receptor antibody-induced myasthenia and a relapsing EAE model. In the latter model, administration of the anti-C6 mAb even after the disease onset was sufficient to prevent the relapse, excluding any effect on disease induction.

We show that systemic administration of an anti-C6 mAb prevents disease in an acute neuromuscular disease model. Critically, the mAb also impacts a chronic CNS disease. A possible explanation for this is that the mAb depletes the animals of free C6 in the circulation and thus prevents influx of C6 into the brain in areas of BBB breakdown. Since the liver is the main source of C6 production [46] and no expression of *C6* mRNA was seen in studies on post-mortem human brain (GTEx Portal, Gencode ID: ENSG00000039537.13; https://www.gtexportal.org/home/gene/ENSG00000039537.13%09), a direct role for the mAb in the CNS is unlikely unless there is significant BBB leakage. Block of C6 influx prevents MAC formation not only in the CNS, a damaging event that occurs on apoptotic cells and debris [58, 59], but also on neoepitopes exposed after trauma, propagating injury [60]. It is also possible that systemic C6 depletion prevents MAC-induced endothelial damage. Given that MAC contributes to vascular ruptures by inducing NF-kb-mediated transcription of adhesion and inflammatory molecules to endothelial cells [61] and by attenuating endothelium-dependent relaxation [62], systemic C6 inhibition may prevent CNS damage by maintaining vascular integrity. Finally, systemic C6 blockade may confer protection in neurological disease by modulating the influx of complement-activated lymphocytes into the CNS parenchyma or their activation state within the meninges. MAC/TCC levels are also increased in the CSF of the injured brain [63] possibly due to local activation following leakage of complement components through the damaged vascular and/or meningeal barriers. The RNAseq data presented in this paper are in line with reported effects of C6 inhibition on the severity of neuroinflammation in a Biozzi crEAE model [17]. Since meningeal inflammation is a critical process in MS pathology [64], the possibility that this is regulated by complement-dependent pathways is of significant interest and must be studied further. The contribution of the terminal pathway in the different disease models varies. In the EMAG model, C6 inhibition can prevent disease. In the PVG crEAE model, the contribution of the complement pathway is less since the disease can be induced in C6-deficient rats, but the relapse is suppressed, and the 7E5 mAb treatment reduces it to the same level.

The C6-binding mAb CP010 presented in this study impedes complement activation in vitro and in vivo by inhibiting the terminal pathway. Our structural analysis revealed a large and highly charged interface between the CP010 Fab fragment and the FIM1-2 domains of C6 matching well the low K_D value for the interaction. The structure also allowed us to predict whether CP010 will interact strongly with C6 from other mammals.

Our biochemical and crystallographic studies demonstrated that CP010 binds the FIM2 domain of C6 and prevents the reversible interaction between C6 and C5/C5b by blocking the FIM1-2:C5 C345c axis. In support of this, a prior study demonstrated that recombinant C5 C345c inhibits haemolytic activity and interacts strongly with

both C6 and C7 [51]. The FIM domains of C6 are indispensable for the reversible binding to native C5; however, they are not strictly required for C6 haemolytic activity [52] nor are they necessary for the stability of the C5b6 complex. However, it is not yet known whether C5 and C6 remain weakly associated during cleavage of C5 to C5b by a C5 convertase before formation of the highly stable C5b6 complex or if C6 is immediately captured by C5b after cleavage. Indeed, the very short half-life of C5b (2 min) [5] suggest that association must happen rapidly after C5 activation. Indeed, the reversible C5:C6 interaction would increase the local concentration of C6 around nascent C5b, thus lowering the threshold for MAC formation in plasma [51]. The C6 FIM domains themselves are not essential for MAC assembly, but inhibition of FIM domain-dependent contacts by removal of these domains or with the CP010 antibody attenuates C5/C5b interactions with C6.

Our CP010 mAb provides a novel route to controlling complement activity downstream of C5 in diseases. Several C6 antibodies have been developed to date, but only two published antibody are described that blocks MAC activity. Only blockers out of 20 C6-reactive mAbs were identified by Lin et al. [65], suggesting that inhibitory epitopes in C6 may be difficult to raise antibodies against [49, 50]. This mAb, named 1C9, inhibited MAC formation by preventing binding of C7 to existing C5b6 complexes, but its C6 epitope was not determined. Like CP010, 1C9 also binds free C6 but may not prevent C5b6 complex formation. Another study describes a C6-binding antibody, WU 6-4, which binds to the third thrombospondin domain and interferes with C5b6 formation [66]. This antibody binds only free C6 and does not detect C5b6 or TCC.

In summary, we have developed a humanized C6 specific antibody that blocks MAC assembly. Systemic administration of this antibody at a therapeutically relevant dose can prevent MAC formation and disease progression in complement-mediated disease by complexing all free C6 from the circulation. Since the majority, if not all, of C6 is made outside the CNS, it can be applied systemically to prevent MAC formation in CNS disease, while leaving the C5a axis intact.

Acknowledgements

We thank Nina Woodworth and Malin Hultqvist from Redoxis AB, Lund, Sweden for performing the in vivo animal experiments and Sarah Cramer from StageBio, Frederick, MD, USA, for performing neuropathology.

Statement of Ethics

Animal experiments: All animal experiments were performed in accordance with the Dutch Animal Welfare Law (Wet op Dierproeven: January 12, 1977, revised in 2014 to be in accordance with EU directive [2010/63/EU]) or the Swedish animal welfare laws. This study protocol was reviewed and approved by Animal Ethics Committee; DEC AMC, Amsterdam, the Netherlands, with approval numbers (DNL100368, DNL102743, DNL103081) and Malmö/Lunds djurförsöksetiska named under the Swedish board of agriculture with protocol number (15395-2018 with amendments 2265-2019 and 14576-2020) and protocol (13693-2018). All experiments were monitored by local animal welfare officers. The ARRIVE guidelines were followed in the planning, design, and execution of the animal experiments [67].

Conflict of Interest Statement

Yuchun Zhang, Muhammad Ahasan, Krista K. Johnson, and Yi Wang are employees of Alexion. Kees Fluiter was a paid consultant for Complement Pharma. Frank Baas and Marcus van Dijk are shareholders of Complement Pharma.

Funding Sources

B. Paul Morgan is funded by the UK Dementia Research Institute; Wioleta M. Zelek is funded by a Health and Care Research Wales Fellowship. This work was funded by Regenesance BV, her successor Complement Pharma BV and Alexion, AstraZeneca Rare Disease.

Author Contributions

Yi Wang, Marcus van Dijk, B. Paul Morgan, Gregers Rom Andersen, and Frank Baas designed the studies. Heidi Gytz Olesen, Iliana Michailidou, Wioleta M. Zelek, Jeroen Vreijling, Patrick Ruizendaal, Ferry de Klein, J. Arnoud Marquart, Kees Fluiter, Muhammad Ahasan, Krista K. Johnson, and Yuchun Zhang performed experiments. Thomas B. Kuipers and Hailiang Mei performed data analysis. Heidi Gytz Olesen, Iliana Michailidou, Wioleta M. Zelek, Kees Fluiter, B. Paul Morgan, Gregers Rom Andersen, and Frank Baas wrote the manuscript.

Data Availability Statement

Data generated or analysed during this study are included in this article (and/or) its online supplementary material. Enquiries on data underlying animal studies and neuropathology can be directed to the corresponding author (Frank Baas). Coordinates and structure factors are available at the protein data bank as the entry 7Q6C.

References

1 Dalakas MC, Alexopoulos H, Spaeth PJ. Complement in neurological disorders and emerging complement-targeted therapeutics. Nat Rev Neurol. 2020;16(11):601–17.
2 Tenner AJ, Stevens B, Woodruff TM. New tricks for an ancient system: physiological and pathological roles of complement in the CNS. Mol Immunol. 2018;102:3–13.
3 Ricklin D, Hajishengallis G, Yang K, Lambris JD. Complement: a key system for immune surveillance and homeostasis. Nat Immunol. 2010;11(9):785–97.
4 Bayly-Jones C, Bubeck D, Dunstone MA. The mystery behind membrane insertion: a review of the complement membrane attack complex. Philos Trans R Soc Lond B Biol Sci. 2017; 372(1726):20160221.
5 Cooper NR, Müller-Eberhard HJ. The reaction mechanism of human C5 in immune hemolysis. J Exp Med. 1970;132(4):775–93.
6 Laudisi F, Spreafico R, Evrard M, Hughes TR, Mandriani B, Kandasamy M, et al. Cutting edge: the NLRP3 inflammasome links complement-mediated inflammation and IL-1β release. J Immunol. 2013 Aug 1;191(3):1006–10.
7 Triantafilou K, Hughes TR, Triantafilou M, Morgan BP. The complement membrane attack complex triggers intracellular Ca2+ fluxes leading to NLRP3 inflammasome activation. J Cell Sci. 2013 Jul 1;126(Pt 13):2903–13.
8 Hammad A, Westacott L, Zaben M. The role of the complement system in traumatic brain injury: a review. J Neuroinflammation. 2018; 15(1):24.
9 Stahel PF, Morganti-Kossmann MC, Kossmann T. The role of the complement system in traumatic brain injury. Brain Res Brain Res Rev. 1998;27(3):243–56.
10 Koski CL, Sanders ME, Swoveland PT, Lawley TJ, Shin ML, Frank MM, et al. Activation of terminal components of complement in patients with Guillain-Barré syndrome and other demyelinating neuropathies. J Clin Invest. 1987 Nov;80(5):1492–7.
11 Mullins RF, Schoo DP, Sohn EH, Flamme-Wiese MJ, Workamelahu G, Johnston RM, et al. The membrane attack complex in aging human choriocapillaris: relationship to macular degeneration and choroidal thinning. Am J Pathol. 2014 Nov;184(11):3142–53.
12 Ramaglia V, Tannemaat MR, de Kok M, Wolterman R, Vigar MA, King RH, et al. Complement inhibition accelerates regeneration in a model of peripheral nerve injury. Mol Immunol. 2009 Dec;47(2–3):302–9.
13 Ramaglia V, King RH, Nourallah M, Wolterman R, de Jonge R, Ramkema M, et al. The membrane attack complex of the complement system is essential for rapid Wallerian degeneration. J Neurosci. 2007 Jul 18;27(29): 7663–72.
14 Sehgal A, Vaishnaw A, Fitzgerald K. Liver as a target for oligonucleotide therapeutics. J Hepatol. 2013;59(6):1354–9.
15 Fluiter K, Opperhuizen AL, Morgan BP, Baas F, Ramaglia V. Inhibition of the membrane attack complex of the complement system reduces secondary neuroaxonal loss and promotes neurologic recovery after traumatic brain injury in mice. J Immunol. 2014 Mar 1; 192(5):2339–48.
16 Bahia El Idrissi N, Das PK, Fluiter K, Rosa PS, Vreijling J, Troost D, et al. M. leprae components induce nerve damage by complement activation: identification of lipoarabinomannan as the dominant complement activator. Acta Neuropathol. 2015 May;129(5):653–67.
17 Michailidou I, Jongejan A, Vreijling JP, Georgakopoulou T, de Wissel MB, Wolterman RA, et al. Systemic inhibition of the membrane attack complex impedes neuroinflammation in chronic relapsing experimental autoimmune encephalomyelitis. Acta Neuropathol Commun. 2018 May 3;6(1):36.
18 Volanakis JE. The role of complement in innate and adaptive immunity. In: Cooper MD, Koprowski H, editors. The interface between innate and acquired immunity. Berlin, Heidelberg: Springer Berlin Heidelberg; 2002. p. 41–56.
19 Hajishengallis G, Reis ES, Mastellos DC, Ricklin D, Lambris JD. Novel mechanisms and functions of complement. Nat Immunol. 2017 Nov 16;18(12):1288–98.
20 Dunkelberger JR, Song WC. Complement and its role in innate and adaptive immune responses. Cell Res. 2010;20(1):34–50.
21 Lee JW, Sicre de Fontbrune F, Wong Lee Lee L, Pessoa V, Gualandro S, Füreder W, et al. Ravulizumab (ALXN1210) vs eculizumab in adult patients with PNH naive to complement inhibitors: the 301 study. Blood. 2019 Feb 7; 133(6):530–9.
22 Mastellos DC, Deangelis RA, Lambris JD. Complement-triggered pathways orchestrate regenerative responses throughout phylogenesis. Semin Immunol. 2013;25(1):29–38.
23 Guo RF, Ward PA. Role of C5a in inflammatory responses. Annu Rev Immunol. 2005;23: 821–52.
24 Woodruff TM, Ager RR, Tenner AJ, Noakes PG, Taylor SM. The role of the complement system and the activation fragment C5a in the central nervous system. Neuromolecular Med. 2010 Jun;12(2):179–92.
25 Doenecke A, Winnacker EL, Hallek M. Rapid amplification of cDNA ends (RACE) improves the PCR-based isolation of immunoglobulin variable region genes from murine and human lymphoma cells and cell lines. Leukemia. 1997;11(10):1787–92.
26 Bradbury A. Cloning hybridoma cDNA by RACE. In: Kontermann R, Dübel S, editors. Antibody engineering. Berlin, Heidelberg: Springer Berlin Heidelberg; 2001. p. 56–61.
27 Hwang WY, Almagro JC, Buss TN, Tan P, Foote J. Use of human germline genes in a CDR homology-based approach to antibody humanization. Methods. 2005 May;36(1):35–42.
28 Wu H, Pfarr DS, Johnson S, Brewah YA, Woods RM, Patel NK, et al. Development of motavizumab, an ultra-potent antibody for the prevention of respiratory syncytial virus infection in the upper and lower respiratory tract. J Mol Biol. 2007 May 4;368(3):652–65.
29 Schlothauer T, Herter S, Koller CF, Grau-Richards S, Steinhart V, Spick C, et al. Novel human IgG1 and IgG4 Fc-engineered antibodies with completely abolished immune effector functions. Protein Eng Des Sel. 2016 Oct;29(10):457–66.
30 Schatz-Jakobsen JA, Zhang Y, Johnson K, Neill A, Sheridan D, Andersen GR. Structural basis for eculizumab-mediated inhibition of the complement terminal pathway. J Immunol. 2016 Jul 1;197(1):337–44.
31 Laursen NS, Gordon N, Hermans S, Lorenz N, Jackson N, Wines B, et al. Structural basis for inhibition of complement C5 by the SSL7 protein from Staphylococcus aureus. Proc Natl Acad Sci U S A. 2010 Feb 23;107(8): 3681–6.
32 Kabsch W. XDS. Acta Crystallogr D Biol Crystallogr. 2010;66(Pt 2):125–32.
33 Dunbar J, Krawczyk K, Leem J, Baker T, Fuchs A, Georges G, et al. SAbDab: the structural antibody database. Nucleic Acids Res. 2014 Jan;42(Database issue):D1140–6.
34 McCoy AJ, Grosse-Kunstleve RW, Adams PD, Winn MD, Storoni LC, Read RJ. Phaser crystallographic software. J Appl Crystallogr. 2007 Aug 1;40(Pt 4):658–74.
35 Liebschner D, Afonine PV, Baker ML, Bunkóczi G, Chen VB, Croll TI, et al. Macromolecular structure determination using X-rays, neutrons and electrons: recent developments in Phenix. Acta Crystallogr D Struct Biol. 2019 Oct 1;75(Pt 10):861–77.
36 Emsley P, Cowtan K. Coot: model-building tools for molecular graphics. Acta Crystallogr D Biol Crystallogr. 2004;60(Pt 12 Pt 1):2126–32.
37 van Dixhoorn MG, Timmerman JJ, Van Gijlswijk-Janssen DJ, Muizert Y, Verweij C, Discipio RG, et al. Characterization of complement C6 deficiency in a PVG/c rat strain. Clin Exp Immunol. 1997 Aug;109(2):387–96.
38 Tzartos SJ, Rand DE, Einarson BL, Lindstrom JM. Mapping of surface structures of electrophorus acetylcholine receptor using monoclonal antibodies. J Biol Chem. 1981 Aug 25;256(16):8635–45.
39 Day MJ. Histopathology of EAE. In: Lavi E, Constantinescu CS, editors. Experimental models of multiple sclerosis. Boston, MA: Springer US; 2005. p. 25–43.
40 Dobin A, Davis CA, Schlesinger F, Drenkow J, Zaleski C, Jha S, et al. STAR: ultrafast universal RNA-seq aligner. Bioinformatics. 2013 Jan 1;29(1):15–21.
41 Anders S, Pyl PT, Huber W. HTSeq: a Python framework to work with high-throughput sequencing data. Bioinformatics. 2015;31(2): 166–9.

42 Krämer A, Green J, Pollard J Jr, Tugendreich S. Causal analysis approaches in ingenuity pathway analysis. Bioinformatics. 2014 Feb 15;30(4):523–30.
43 Abarca K, Jung E, Fernández P, Zhao L, Harris B, Connor EM, et al. Safety, tolerability, pharmacokinetics, and immunogenicity of motavizumab, a humanized, enhanced-potency monoclonal antibody for the prevention of respiratory syncytial virus infection in at-risk children. Pediatr Infect Dis J. 2009 Apr;28(4):267–72.
44 Lindstrom JM, Einarson BL, Lennon VA, Seybold ME. Pathological mechanisms in experimental autoimmune myasthenia gravis. I. Immunogenicity of syngeneic muscle acetylcholine receptor and quantitative extraction of receptor and antibody-receptor complexes from muscles of rats with experimental autoimmune myasthenia gravis. J Exp Med. 1976 Sep 1;144(3):726–38.
45 Zelek WM, Morgan BP. Monoclonal antibodies capable of inhibiting complement downstream of C5 in multiple species. Front Immunol. 2020;11:612402.
46 Hobart MJ, Lachmann PJ, Calne RY. C6: synthesis by the liver in vivo. J Exp Med. 1977; 146(2):629–30.
47 Ereño-Orbea J, Sicard T, Cui H, Carson J, Hermans P, Julien JP. Structural basis of enhanced crystallizability induced by a molecular chaperone for antibody antigen-binding fragments. J Mol Biol. 2018 Feb 2;430(3):322–36.
48 North B, Lehmann A, Dunbrack RL Jr. A new clustering of antibody CDR loop conformations. J Mol Biol. 2011;406(2):228–56.
49 Aleshin AE, DiScipio RG, Stec B, Liddington RC. Crystal structure of C5b-6 suggests structural basis for priming assembly of the membrane attack complex. J Biol Chem. 2012 Jun 1;287(23):19642–52.
50 Hadders MA, Bubeck D, Roversi P, Hakobyan S, Forneris F, Morgan BP, et al. Assembly and regulation of the membrane attack complex based on structures of C5b6 and sC5b9. Cell Rep. 2012 Mar 29;1(3):200–7.
51 Thai CT, Ogata RT. Expression and characterization of the C345C/NTR domains of complement components C3 and C5. J Immunol. 2003;171(12):6565–73.
52 DiScipio RG, Linton SM, Rushmere NK. Function of the factor I modules (FIMS) of human complement component C6. J Biol Chem. 1999;274(45):31811–8.
53 DiScipio RG. Formation and structure of the C5b-7 complex of the lytic pathway of complement. J Biol Chem. 1992;267(24):17087–94.
54 Klein RJ, Zeiss C, Chew EY, Tsai JY, Sackler RS, Haynes C, et al. Complement factor H polymorphism in age-related macular degeneration. Science. 2005 Apr 15;308(5720):385–9.
55 Hammond TR, Marsh SE, Stevens B. Immune signaling in neurodegeneration. Immunity. 2019;50(4):955–74.
56 Lambert JC, Heath S, Even G, Campion D, Sleegers K, Hiltunen M, et al. Genome-wide association study identifies variants at CLU and CR1 associated with Alzheimer's disease. Nat Genet. 2009 Oct;41(10):1094–9.
57 Potter PC, Frasch CE, van der Sande WJ, Cooper RC, Patel Y, Orren A. Prophylaxis against Neisseria meningitidis infections and antibody responses in patients with deficiency of the sixth component of complement. J Infect Dis. 1990 May;161(5):932–7.
58 Fraser DA, Pisalyaput K, Tenner AJ. C1q enhances microglial clearance of apoptotic neurons and neuronal blebs, and modulates subsequent inflammatory cytokine production. J Neurochem. 2010;112(3):733–43.
59 Tenner AJ, Robinson SL, Ezekowitz RA. Mannose binding protein (MBP) enhances mononuclear phagocyte function via a receptor that contains the 126,000 M(r) component of the C1q receptor. Immunity. 1995;3(4): 485–93.
60 Narang A, Qiao F, Atkinson C, Zhu H, Yang X, Kulik L, et al. Natural IgM antibodies that bind neoepitopes exposed as a result of spinal cord injury, drive secondary injury by activating complement. J Neuroinflammation. 2017 Jun 19;14(1):120.
61 Kilgore KS, Schmid E, Shanley TP, Flory CM, Maheswari V, Tramontini NL, et al. Sublytic concentrations of the membrane attack complex of complement induce endothelial interleukin-8 and monocyte chemoattractant protein-1 through nuclear factor-kappa B activation. Am J Pathol. 1997 Jun;150(6):2019–31.
62 Stahl GL, Reenstra WR, Frendl G. Complement-mediated loss of endothelium-dependent relaxation of porcine coronary arteries. Role of the terminal membrane attack complex. Circ Res. 1995;76(4):575–83.
63 Tatomir A, Talpos-Caia A, Anselmo F, Kruszewski AM, Boodhoo D, Rus V, et al. The complement system as a biomarker of disease activity and response to treatment in multiple sclerosis. Immunol Res. 2017 Dec;65(6): 1103–9.
64 van Olst L, Rodriguez-Mogeda C, Picon C, Kiljan S, James RE, Kamermans A, et al. Meningeal inflammation in multiple sclerosis induces phenotypic changes in cortical microglia that differentially associate with neurodegeneration. Acta Neuropathol. 2021 Jun; 141(6):881–99.
65 Lin K, Zhang L, Kong M, Yang M, Chen Y, Poptic E, et al. Development of an anti-human complement C6 monoclonal antibody that inhibits the assembly of membrane attack complexes. Blood Adv. 2020 May 12;4(9): 2049–57.
66 Würzner R, Mewar D, Fernie BA, Hobart MJ, Lachmann PJ. Importance of the third thrombospondin repeat of C6 for terminal complement complex assembly. Immunology. 1995 Jun;85(2):214–9.
67 Percie du Sert N, Hurst V, Ahluwalia A, Alam S, Avey MT, Baker M, et al. The ARRIVE guidelines 2.0: updated guidelines for reporting animal research. PLoS Biol. 2020;18(7): e3000410.